

Integral Field Spectroscopy of a sample of nearby galaxies.

I. Sample, Observations and Data Reduction[★]

E. Marmol-Queralto^{1,2}, S.F. Sánchez¹, R.A. Marino^{1,2}, D. Mast^{1,3}, K. Viironen^{1,4}, A. Gil de Paz², J. Iglesias-Páramo^{3,1}, F.F. Rosales-Ortega^{5,1}, and J.M. Vilchez³

¹ Centro Astronómico Hispano Alemán, Calar Alto, (CSIC-MPG), C/Jesús Durbán Remón 2-2, E-04004 Almería, Spain e-mail: emq@astrax.fis.ucm.es

² Departamento de Astrofísica y CC. de la Atmósfera, Universidad Complutense de Madrid, E28040-Madrid, Spain

³ Instituto de Astrofísica de Andalucía (CSIC), Camino Bajo de Huetor s/n, Aptdo. 3004, E18080-Granada, Spain

⁴ Centro de Estudios de Física del Cosmos de Aragón (CEFCA), C/ Pizarro 1, 3^a, E-41001 Teruel, Spain

⁵ Departamento de Física Teórica, Universidad Autónoma de Madrid, E28049-Cantoblanco (Madrid), Spain

Received — ; accepted —

ABSTRACT

Aims. Integral Field Spectroscopy (IFS) is a powerful approach for the study of nearby galaxies since it enables a detailed analysis of their resolved physical properties. Here we present the sample of nearby galaxies selected to exploit the two dimensional information provided by the IFS.

Methods. We observed a sample of 48 galaxies from the Local Universe with the PPAK Integral Field Spectroscopy unit (IFU), of the PMAS spectrograph, mounted at the 3.5 m telescope at Calar Alto Observatory (Almería, Spain). Two different setups were used during these studies (low -V300- and medium -V600- resolution mode) covering a spectral range of around 3700 – 7000 Å. We developed a full automatic pipeline for the data reduction, that includes an analysis of the quality of the final data products. We applied a decoupling method to obtain the ionised gas and stellar content of these galaxies, and to derive the main physical properties of the galaxies. To assess the accuracy in the measurements of the different parameters, we performed a set of simulations to derive the expected relative errors obtained with these data. In addition, we extracted two aperture, central and integrated spectra, from the datacubes. The main properties of the stellar populations and ionised gas of these galaxies and an estimate of their relative errors are derived from those spectra, as well as from the whole datacubes.

Results. The comparison of the central spectrum extracted from the datacubes and the SDSS spectrum for those galaxies in common shows a good agreement between the derived values from both samples. We find differences in the properties of galaxies when comparing a central and an integrated spectra, showing the effects of the extracted aperture in the interpretation of the data. Finally, we present two dimensional maps of some of the main properties derived with the decoupling procedure.

Key words. surveys – techniques: spectroscopic – galaxies: abundances – stars: formation – galaxies: ISM – galaxies: stellar content

1. Introduction

Galaxies in the Local Universe are the final product of their cosmological evolution, and their actual properties are a direct consequence of their assembling, star formation, enrichment and environmental effects (interactions/mergers). Since all these processes are imprinted in the spectral features along their whole extension, a two dimensional analysis can help us to understand the evolution that galaxies have undergone. The use of Integral Field Spectroscopy (IFS) enables us to build two dimensional maps with a detailed characterisation of their spectroscopic properties, and therefore IFS is a powerful tool for the study of nearby galaxies.

In this paper, we present an exploratory study of 48 nearby galaxies observed using the PMAS spectrograph (Postdam Multi Aperture Spectrograph, Roth et al. 2005) in the PPAK mode (Verheijen et al. 2004; Roth et al. 2005), mounted at the 3.5 m telescope of the Centro Astronómico Hispano Alemán (CAHA,

Spain). The wide field-of-view (FOV) of PPAK (74'' × 65'') allows us to sample galaxies in the Local Universe covering most of their optical extent. We have explored two different setups (low and medium spectral resolution) to finally obtain ~ 40000 spectra, covering an area of ~ 50 arcmin². To exploit at maximum the capabilities of this instrument, we have observed galaxies in a redshift range of 0.005 < z < 0.025, in a compromise between the covered area and their sampling (spatial resolution). This redshift range corresponds to a luminosity distances of D_L = 19 – 106 Mpc, and one arcsec would correspond to a linear scale of ~ 92 – 527 pc, assuming a standard Λ CDM cosmology (H₀ = 70.5, Ω = 0.27, Λ = 0.73, Hinshaw et al. 2009). Thus, this study enables to distinguish structures in the galaxies (arms, bars, bulge/disk), although smaller interesting regions, as individual H II regions, will not be resolved with these observations.

Previous works have explored the use of different integral field spectrophotometers for a detailed study of nearby galaxies. In particular, the SAURON project (Bacon et al. 2001; de Zeeuw et al. 2002), and its extension Atlas3D (Cappellari et al. 2011) are focused on the analysis of early-type galaxies and bulges of spirals at z < 0.01, to study their kinemat-

[★] Based on observations collected at the Centro Astronómico Hispano Alemán (CAHA) at Calar Alto, operated jointly by the Max-Planck Institut für Astronomie and the Instituto de Astrofísica de Andalucía (CSIC).

ics and stellar populations. Due to the distance of their objects ($D_L < 42$ Mpc) and the FOV covered by the SAURON instrument ($33'' \times 41''$), this study is mainly restricted to the central part of galaxies. The study of nearby spiral galaxies has been addressed by the VENGA survey (32 nearby spiral galaxies, Blanc et al. 2010) using the VIRUS-P spectrograph (Hill et al. 2008), the DiskMass Survey (Bershady et al. 2010a, 146 nearby face-on galaxies) combining PPAK and the SparsePak spectrograph (Bershady et al. 2004, 2005), and the PINGS survey (17 nearby disk galaxies, Rosales-Ortega et al. 2010), using PPAK, as in this work. In particular, the mosaicking designed for the PINGS survey allowed to map the H II regions along the whole extension their galaxies and to explore the two-dimensional metallicity structure of disks. Our sample comprises galaxies of different morphological types in the considered redshift range, with predominance of spiral galaxies. In addition, they were selected in size to fit in the FOV of the PPAK instrument, and therefore, to map their physical properties in their whole extension in just one pointing. The results obtained from the PING survey can be compared with the work presented in this article to analyse the distance effects in determination and interpretation of their physical properties.

The sample selection, observational strategy, data reduction and analysis of the accuracy of the final data set presented here formed part of the exploratory studies for the final selection for the optimal instrumental setup and sample of the CALIFA survey (Calar Alto Legacy Integral Field spectroscopy Area survey¹, Sánchez et al. 2010, 2011a). CALIFA is an ongoing survey for observing ~ 600 nearby galaxies to explore the mechanisms who drives their evolution along the colour-magnitude diagram by studying their kinematics, ionised gas and stellar content. As part of this work, we have performed a wide set of simulations to check the quality of the data and the recovering of the physical properties of the observed galaxies. Although this analysis has produced a bench mark for the observational strategy and data reduction scheme for future samples, e.g. in the CALIFA survey, the data described in this article comprise a well separated data set, which contains interesting physical information of the considered galaxies, and therefore we present them as a separated study.

In this paper we focus on the sample (§ 2), observations (§ 3), and data reduction (§ 4). The first analysis and results from these data, including a detailed study of the accuracy of the derived physical parameters from the simulations, are presented in § 5. Further analysis for different aspects of galaxies, as the properties of the ionised gas, and particular interesting objects will be presented in forthcoming papers.

2. Sample

Two different sample selections have been explored in this work: (1) galaxies extracted from the SDSS DR4 imaging sample brighter than $r < 15.75$ mag, at a redshift slice between $0.005 < z < 0.025$ (selection in volume and limiting magnitude) and (2) face-on disk galaxies included in the DiskMass Survey (DMS, Bershady et al. 2010a, Verheijen, private communications) with appropriate sizes to fill the field-of-view (FOV) of the instrument (angular isophotal diameter selection). The first criterion is the standard method to select galaxies at a redshift range. In this case, the angular size of each galaxy is different and, therefore the two dimensional information available for the sample is limited. On the other hand, the face-on galaxy sub-sample was

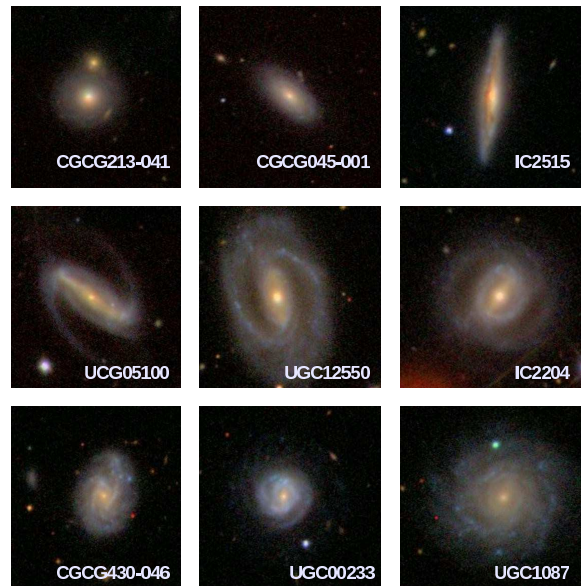


Fig. 1. Subset of 9 of the observed galaxies, where the difference in projected sizes can be seen. All images are $1.5' \times 1.5'$ (north is up, east to left). Images from SDSS survey.

selected to solve this problem, but in this case the sample is not complete and representative of the Local Universe, and particular care has to be taken when interpreting the results in terms of global evolution.

In total, a subset of 48 galaxies were finally observed, randomly selected from those two samples depending on their visibility at the considered nights. Four galaxies were partially observed and they are not included in this work. Table 1 lists the observed galaxies, including some basic information as the name, coordinates, a basic morphological classification (when available), redshift, and V -band absolute magnitudes. Although there is a bias towards gas-rich late-type galaxies due to the selection of the sample, it is an heterogeneous sample that includes bulge-dominated and almost pure-disk galaxies, face-on and edge-on objects, and galaxies with and without bars. This is shown in Fig. 1, where some galaxies included in this study (images from the SDSS catalogue) are presented.

Finally, we present in Figure 2 the colour-magnitude diagram of the observed objects, indicating those ones coming from each sub-sample. Regions corresponding to the red sequence, the green valley and the blue cloud are also indicated (e.g., Strateva et al. 2001; Bell et al. 2004, 2006; Faber et al. 2007; Chen et al. 2010). Although the sample presented here is small, there is a significant number observed galaxies in both the red sequence and the blue cloud, as well as the green valley. Therefore, this sample will allow a preliminary study of the global evolution of galaxies in the Local Universe.

3. Observations

Observations were carried out during 15 nights in several observing runs. Information related to the weather condition during the observations are presented in Table 2. The full sample was observed at the 3.5 m telescope of the Calar

¹ <http://www.caha.es/CALIFA/>

Galaxy	RA (J2000)	DEC (J2000)	Type	z	R_{25} (mag)	M_V (mag)	(B-V) (mag)	ObservingDate (yy-mm-dd)	Grid	Seeing ($''$)	Airmass (mag)
(1)	(2)	(3)	(4)	(5)	(6)	(7)	(8)	(9)	(10)	(11)	(12)
KUG 1033+403	10 ^h 36 ^m 12.4 ^s	+40°03' 12.6 ^{''}	S?	0.0229	0.56	16.5	0.87	2009-03-23	V300	...	1.12
2MASX J13062093+5318232 †	13 ^h 06 ^m 21.0 ^s	+53°18' 23.2 ^{''}	AGN	0.0237	...	15.9	1.25	2009-03-22	V300	2.0	1.11
2MASX J13193595+5330102 †	13 ^h 19 ^m 35.9 ^s	+53°30' 09.8 ^{''}	IrS	0.0248	...	12.4	0.72	2009-03-24	V300	2.0	1.13
CGCG 045-001	13 ^h 30 ^m 43.5 ^s	+07°31' 48.8 ^{''}	...	0.0220	...	15.4	1.07	2009-03-20	V300	1.3	1.19
CGCG 071-096 †	13 ^h 00 ^m 33.2 ^s	+10°07' 47.8 ^{''}	...	0.0239	...	15.1	0.79	2009-03-20	V300	1.1	1.25
CGCG 148-006 †	07 ^h 44 ^m 57.4 ^s	+28°55' 39.0 ^{''}	...	0.0234	...	15.3	0.75	2009-10-23	V600	1.1	1.30
CGCG 181-068 †	09 ^h 37 ^m 19.2 ^s	+33°49' 25.8 ^{''}	...	0.0227	...	15.7	1.17	2009-03-20	V300	1.2	1.06
CGCG 213-041 †	11 ^h 21 ^m 16.8 ^s	+40°20' 43.4 ^{''}	...	0.0208	...	15.5	1.16	2009-03-21	V300	1.7	1.04
CGCG 293-023 †	02 ^h 30 ^m 21.5 ^s	+56°47' 29.5 ^{''}	...	0.0156	...	15.6	0.99	2009-03-23	V300	...	1.18
CGCG 428-059 †	22 ^h 14 ^m 51.4 ^s	+13°42' 54.9 ^{''}	...	0.0242	...	15.7	0.90	2009-06-27	V300	1.0	1.28
CGCG 428-060	22 ^h 14 ^m 57.9 ^s	+13°45' 42.9 ^{''}	...	0.0242	...	13.7	0.92	2009-06-28	V300	1.2	1.21
CGCG 430-046 †	23 ^h 00 ^m 46.2 ^s	+13°37' 07.9 ^{''}	...	0.0243	...	15.3	0.86	2009-10-23	V600	1.1	1.10
IC 2204 †	07 ^h 41 ^m 18.1 ^s	+34°13' 55.9 ^{''}	(R)SB(r)ab	0.0155	0.00	14.6	0.93	2009-10-22	V600	1.5	1.12
IC 2500 †	09 ^h 42 ^m 23.4 ^s	+36°20' 59.1 ^{''}	...	0.0221	...	15.2	1.17	2009-03-21	V300	1.7	1.14
IC 2515 †	09 ^h 54 ^m 39.4 ^s	+37°24' 30.8 ^{''}	Sb	0.0193	0.72	15.1	1.11	2009-03-22	V300	1.6	1.05
MRK 1477 †	13 ^h 16 ^m 14.7 ^s	+41°29' 40.1 ^{''}	...	0.0207	...	15.4	0.47	2009-03-24	V300	1.8	1.04
NGC 99 †,★	00 ^h 23 ^m 59.5 ^s	+15°46' 13.7 ^{''}	Scd	0.0177	0.04	14.0	0.62	2009-10-22	V600	2.3	1.11
NGC 3820 †	11 ^h 42 ^m 04.9 ^s	+10°23' 03.3 ^{''}	S?	0.0203	0.17	14.9	0.95	2009-03-22	V300	1.2	1.40
NGC 4109 †,★	12 ^h 06 ^m 51.1 ^s	+42°59' 44.3 ^{''}	SA?	0.0235	0.05	14.8	0.98	2009-03-19	V300	...	1.05
NGC 7570 †,★	23 ^h 16 ^m 44.7 ^s	+13°28' 58.8 ^{''}	SBa	0.0157	0.23	13.9	0.81	2009-10-22	V600	2.0	1.13
UGC 74	00 ^h 08 ^m 44.7 ^s	+04°36' 45.1 ^{''}	SAB(rs)c?	0.0131	0.05	14.5	0.85	2009-10-17	V600	1.3	1.23
UGC 233	00 ^h 24 ^m 42.7 ^s	+14°49' 28.8 ^{''}	SBbc D	0.0176	0.00	14.6	0.62	2009-10-23	V600	1.1	1.20
UGC 448	00 ^h 42 ^m 22.0 ^s	+29°38' 29.9 ^{''}	SABc	0.0162	0.04	14.4	1.16	2009-10-19	V600	2.0	1.08
UGC 463 †	00 ^h 43 ^m 32.4 ^s	+14°20' 33.2 ^{''}	SAB(rs)c	0.0148	0.00	13.5	0.85	2009-10-18	V600	1.8	1.29
UGC 1081	01 ^h 30 ^m 46.6 ^s	+21°26' 25.5 ^{''}	SB(rs)c	0.0104	0.03	13.8	0.83	2009-10-22	V600	2.4	1.15
UGC 1087 †	01 ^h 31 ^m 26.6 ^s	+14°16' 39.0 ^{''}	SA(rs)c	0.0149	0.03	15.1	0.69	2009-10-17	V600	1.0	1.13
UGC 1529	02 ^h 02 ^m 31.0 ^s	+11°05' 35.1 ^{''}	SA(rs)c	0.0155	0.07	14.7	1.01	2009-10-18	V600	1.5	1.17
UGC 1635	02 ^h 08 ^m 27.7 ^s	+06°23' 41.7 ^{''}	SABc	0.0115	0.01	14.8	0.96	2009-10-23	V600	1.2	1.10
UGC 1862	02 ^h 24 ^m 24.8 ^s	-02°09' 44.5 ^{''}	SAB(rs)d pec?	0.0046	0.11	14.0	0.83	2009-10-23	V600	1.3	1.20
UGC 3091	04 ^h 33 ^m 56.1 ^s	+01°06' 49.5 ^{''}	SAB(s)d?	0.0184	...	15.4	0.88	2009-10-17	V600	0.9	1.40
UGC 3140	04 ^h 42 ^m 54.9 ^s	+00°37' 06.9 ^{''}	SA(rs)c?	0.0154	0.06	13.6	0.97	2009-10-19	V600	1.8	1.36
UGC 3701	07 ^h 11 ^m 42.7 ^s	+72°10' 09.5 ^{''}	SA(rs)cd?	0.0097	0.00	15.2	0.87	2009-10-17	V600	1.5	1.30
UGC 3997 ★	07 ^h 44 ^m 38.7 ^s	+40°21' 58.5 ^{''}	Im?	0.0197	0.06	16.0	1.07	2009-10-18	V600	1.5	1.13
UGC 4036	07 ^h 51 ^m 54.7 ^s	+73°00' 56.5 ^{''}	SAB(r)b?	0.0116	0.06	12.7	0.98	2009-10-19	V600	1.6	1.38
UGC 4107	07 ^h 57 ^m 01.9 ^s	+49°34' 02.5 ^{''}	SA(rs)c	0.0117	0.01	13.9	1.06	2009-10-22	V600	1.2	1.13
UGC 5100 †	09 ^h 34 ^m 38.6 ^s	+05°50' 29.9 ^{''}	SB(s)b	0.0184	0.22	14.9	1.02	2009-03-19	V300	1.1	1.23
UGC 6156 †	11 ^h 06 ^m 31.3 ^s	+48°39' 05.7 ^{''}	S?	0.0245	0.56	15.1	0.54	2009-03-24	V300	1.5	1.11
UGC 6410 †	11 ^h 24 ^m 05.9 ^s	+45°48' 39.9 ^{''}	SABc	0.0187	0.11	14.8	0.78	2009-03-20	V300	1.5	1.08
UGC 7993 †	12 ^h 50 ^m 31.6 ^s	+52°07' 22.5 ^{''}	Scd?	0.0161	0.90	15.3	0.79	2009-03-19	V300	1.3	1.25
UGC 9837 †	15 ^h 23 ^m 51.7 ^s	+58°03' 10.6 ^{''}	SAB(s)c	0.0089	0.02	14.6	0.57	2007-06-23	V300	...	1.10
UGC 9965	15 ^h 40 ^m 06.7 ^s	+20°40' 50.2 ^{''}	SA(rs)c	0.0151	0.06	14.4	0.72	2007-06-22	V300	...	1.39
UGC 11318	18 ^h 39 ^m 12.2 ^s	+55°38' 30.5 ^{''}	SB(rs)bc	0.0196	0.03	14.1	0.72	2007-06-23	V300	...	1.10
UGC 12250 †	22 ^h 55 ^m 35.9 ^s	+12°47' 25.1 ^{''}	SBb	0.0242	0.22	14.1	1.04	2009-10-18	V600	1.1	1.33
UGC 12391	23 ^h 08 ^m 57.2 ^s	+12°02' 52.9 ^{''}	SAB(s)c	0.0163	0.04	14.7	0.77	2009-10-17	V600	1.5	1.20

Table 1. General information about the observed galaxies. All the galaxies are included in 2MASS^a. Galaxies marked with † have available SDSS spectroscopy. Galaxies marked with ★ have been observed with GALEX^b.

(1) Galaxy identification; Coordinates: (2) Right ascension and (3) Declination in J2000 Equinox from NED^c; (4) Morphological type from RC3 catalogue^d; (5) Redshift from NED; (6) R_{25} : Radius where the surface brightness reaches $\mu_B = 25.0$ mag/arcsec², obtained from RC3 catalogue; (7) M_V : Absolute B-band magnitude from NED; (8) (B-V); (9) Observing date; (10) PPAK mode utilised for each observation (see Table 3); (11) Average seeing value during the corresponding night observation. Data from the Calar Alto Observatory archive. (12) Airmass for the each observation.

^a Two Micron All Sky Survey (Skrutskie et al. 2006): <http://www.ipac.caltech.edu/2mass/>

^b The GALEX Ultraviolet Atlas of Nearby Galaxies (Gil de Paz et al. 2007)

^c NASA/IPAC Extragalactic Database: <http://nedwww.ipac.caltech.edu/>

^d Third Reference Catalogue of Bright Galaxies: <http://vizier.u-strasbg.fr/viz-bin/VizieR?-source=VII/155>

Alto observatory with PMAS spectrograph (Postdam Multi Aperture Spectrograph, Roth et al. 2005) in the PPAK mode (Verheijen et al. 2004; Roth et al. 2005). The PPAK fibre bundle consists of 382 fibres of 2.7 $''$ diameter each (see Fig. 5 in Roth et al. 2005). The science fibres (331 fibres) are concentrated in a single hexagonal bundle, with a filling factor of ~ 65 %. The sky background is sampled by 36 additional fibres, distributed in 6 bundles of 6 fibres each, distributed along a circle $\sim 90''$ from the centre of the instrument FOV. The sky-fibres are distributed among the science fibres within the pseudo-slit in

order to have a good characterisation of the sky; the remaining 15 fibres are used for calibration purposes.

A dithering scheme with three pointings was adopted during the different observing runs, in order to cover the complete FOV of the bundle and to increase the spatial resolution of the data. This scheme has been already adopted in previous studies using PPAK, with a considerable increase in the quality of the data (e.g., Sánchez et al. 2007b; Castillo-Morales et al. 2010; Pérez-Gallego et al. 2010; Rosales-Ortega et al. 2010). The offsets in RA-dec of the different pointings, with respect to the nominal coordinates of the targets, were (in arcsec): (1) (0, 0), (2)

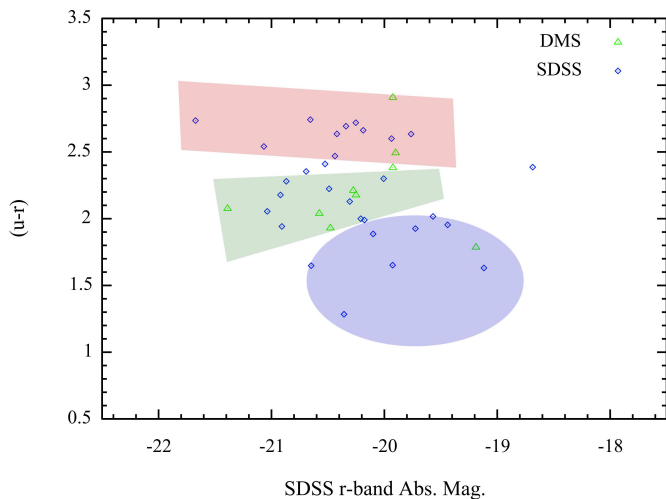


Fig. 2. $u-r$ vs. M_r colour-magnitude diagram of the observed sample. In blue circles we have indicated the DR4 selected sample, and in green triangles those galaxies from the Disk Mass Survey (see text for more detail). The red sequence, green valley and blue cloud are noted with shaded colour areas. It is clear the observed sample still covers each region with a significant number of objects.

Table 2. Atmospheric conditions during the observations. For each night, we present average values of the seeing, humidity, transparency of the atmosphere, and the extinction in the V -band.

Observing date	Seeing (")	Humidity (%)	Transparency (%)	Extinction in V -band (mag)	
2007-06-22*	Clear	–	56	95	0.22
2007-06-23*	Clear	–	48	95	0.22
2009-03-19	Clear	1.2	43	95	0.15
2009-03-20	Clear	1.3	62	85	0.25
2009-03-21	Clouds	1.7	71	75	0.28
2009-03-22	Clear	2.0	70	95	0.15
2009-03-23*	Clouds	–	47	75	0.25
2009-03-24	Clouds	1.8	62	65	0.25
2009-06-27	Clear	1.0	44	95	0.20
2009-06-28	Clear	1.2	70	90	0.20
2009-10-17	Clouds	1.2	79	85	0.25
2009-10-18	Clouds	1.5	58	70	0.30
2009-10-19	Clouds	1.8	75	75	0.20
2009-10-22	Clear	1.6	86	90	0.20
2009-10-23	Clear	1.2	50	95	0.15

*Due to technical problems, there are not data from the seeing monitor for these nights.

Table 3. PMAS/PPAK instrumental setups.

Grid type	V300	V600
Spectral coverage	3620–7056 ÅÅ	3845–7014 ÅÅ
Dispersion	3.2 Å/px	1.5 Å/px
FWHM ^a	10.7 Å	5.4 Å
Exposure time ^b	600 s × 3	600 s × 3

Notes. (a) Spectral resolution (FWHM) for PPAK IFU with 150 μm fibers. (b) Exposure time for each dithering pointing.

(+1.56, +0.78) and (3) (+1.56, –0.78), which allows to cover the holes between fibers in the central bundle. The spatial re-composition of the three pointings is included in the standard data reduction scheme adopted for these data (described in § 4).

Two different setups were used during these observations, listed in Table 3. For the runs before October 2010, it was used

the V300 grating, with a nominal spectral resolution of ~ 10.7 Å (Full Width at Half Maximum –FWHM) and a wavelength range of $\lambda\lambda 3620 - 7056$ ÅÅ. All the targets observed during this run correspond to the first sub-sample described in the previous section. After that date, the V600 grating was used, with a nominal resolution of ~ 5.4 Å (FWHM) and a wavelength range of $\lambda\lambda 3845 - 7014$ ÅÅ. Most of the targets observed during this run correspond to the DMS sub-sample. The main reason for that change was the upgrade of the PMAS CCD, from a $2\text{k} \times 4\text{k}$ chip to a $4\text{k} \times 4\text{k}$ chip, that nominally increases the wavelength range by a factor two at the same spectral resolution. This increase was hampered by a vignetting effect that affects to a ~ 30 % of the fibers/spectra, at the edges of the CCD (see Fig. 3). Fibers positioning in the entrance slit are in such a way that the central and outer regions of the hexagon are located in the central regions of the slit, while the outer regions of the slit corresponds to an annular ring at about $\sim 15''$ from the centre of the IFU. Despite this effect, all the fibers present unvignetting more than ~ 50 % of their spectral range.

4. Data reduction

The large amount of data generated in IFS observations made that the establishment of a precise and quick procedure for the data reduction was one of the key points to test during this study. The reduction was performed using a fully automatic pipeline, that operates without human intervention, producing both the scientific useful frames and a set of quality control measurements (on a web-based interface). The pipeline was based on the routines included in the R3D (Sánchez 2006) and E3D (Sánchez 2004) packages. The reduction consists of the standard steps for fibre-based integral-field spectroscopy. For the V300 data, a master bias frame was created by averaging all the bias frames observed during the night and subtracted from the science frames. In the case of the V600, observed with the new PMAS CCD, which has basically no structure in the bias, a single value bias-level (derived on the basis of the over-scan values), is subtracted to the frames. The different exposures taken at the same position on the sky were then combined, clipping the cosmic rays using IRAF² routines. The next step was to determine the locations of the spectra on the CCD, using in this case a continuum illuminated exposure taken before the science exposures. Each spectrum was then extracted from the science frames.

In order to reduce the effects of the cross-talk, we adopted a modified version of the Gaussian-suppression proposed by Sánchez (2006), and fully described in Sánchez et al. (2011b). This technique assumes a Gaussian profile for the projection of each fibre spectrum along the cross-dispersion axis, and it performs a Gaussian fitting to each of the fibres after subtracting the contribution of the adjacent fibres in an iterative process. The cross-talk is reduced to less than a 1 % when adopting this method.

Each spectrum extracted along the dispersion direction is stored in a row-stacked-spectrum file (RSS, Sánchez 2004). Wavelength calibration was performed using HeHgCd lamp exposures obtained before and after each pointing, yielding an ac-

² IRAF is distributed by the National Optical Astronomy Observatories, which are operated by the Association of Universities for Research in Astronomy, Inc., under cooperative agreement with the National Science Foundation.

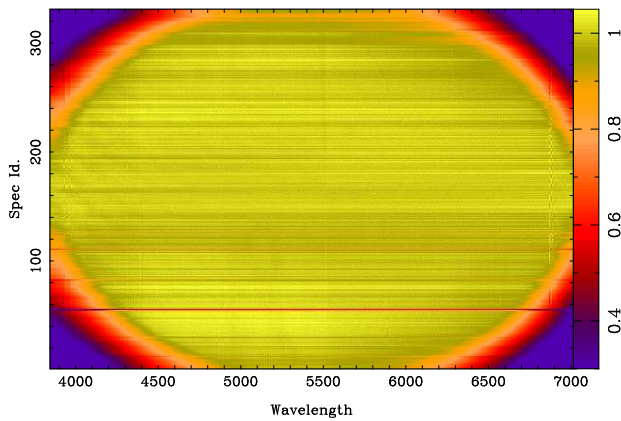


Fig. 3. Intensity map of the differential transmission fiber-to-fiber for the V600 grating. The drop of the transmission at the edges of the image is due to the vignetting. The $\sim 15\%$ of the CCD is affected this effect.

curacy of $\sim 10\%$ of the nominal pixel scale (i.e., $\sim 0.3 \text{ \AA}$ for the V300 grating and $\sim 0.15 \text{ \AA}$ for the V600 one). Differences in the relative fibre-to-fibre transmission throughput were corrected by comparing the wavelength-calibrated RSS science frames with the corresponding frames derived from sky exposures taken during the twilight.

As mentioned before, PPAK is equipped with 36 fibres to sample the sky, distributed around the science fiber-bundle, in six small bundles of six fibers each one, at a distance of $\sim 75''$ from the centre of the FOV (seen Fig. 5 in Kelz et al. 2006). The objects selected to observe in these studies cover a substantial fraction of the FOV of the central PPAK bundle, but most of the sky fibers are free from emission by the targets. The procedure adopted to derive the night-sky spectrum was to combine the spectra corresponding to these fibers, performing a 2σ clipping rejection to remove any possible contamination³. Finally, the sky-spectrum was subtracted to all the spectra the corresponding frame.

Spectrophotometric standard stars from Oke (1990) were observed during the nights to perform the flux calibration. The extracted spectra of these stars were compared with the flux calibrated spectra available in the webpage of the observatory⁴, obtaining the transformation function from observed counts to intensity. In this step, the routines in R3D package take into account the airmass and extinction of the observation of both the spectrophotometric standard stars and the science targets. This procedure ensures a good relative flux calibration from the blue to the red part of the spectra, if the weather conditions along the night were stable. However, an absolute offset between the derived and real fluxes are expected due to the incomplete spatial coverage of the FOV in the observations of the calibration star despite the large fiber size of PPAK ($2.7''$), and second order effects like small inaccuracies in the centering of the star and the effects of the variation of the seeing.

After reducing the frames corresponding to each particular pointing, the science spectra corresponding to the three dithered exposures were combined in a single frame of 993 spectra. In order to take into account possible variations in the atmosphere

³ We adopted this criterion since a 3σ clipping rejection does not remove the contamination by stars in the field, external regions of the galaxies, or a companion galaxy in IFU observations, due to the positions of the fibers.

⁴ <http://www.caha.es/pedraz/SSS/Oke/oke.html>

transmission during the exposures, the procedure rescales the spectra to a common intensity by comparing the integrated spectra within an aperture of $20''$ diameter, chosen in a compromise between the signal-to-noise and the depth of the images, and to avoid seeing effects. The final position tables for the individual fibers are generated taking into account their relative positions to the PPAK central bundle and the offsets provided for the dither scheme. The information included in the combined spectra and position tables are used to create the final datacube.

Next step in the reduction process is to perform the differential atmospheric refraction (DAR) correction. To perform this correction, the pipeline creates a 2D image by co-adding the flux within $4500 - 5500 \text{ \AA}$ (approximately the V-band), and looks for the peak emission within a region between $[15:62, 15:62]$ pixels. This centroid is used as initial reference, that will look for any shift in this centroid along the wavelength within a box of 6×6 pixels. Once the shift is determined, a polynomial order fitting of order 3 is applied to smooth the correction, and the shift is applied wavelength to wavelength, re-centering the cube and correcting for the DAR.

In order to get the best possible absolute flux calibration, we re-calibrated our data using SDSS photometry, whenever is available (37 targets, 33 of them with quality enough for the analysis). Of the five SDSS filters (*ugriz*), our spectrum covers the passbands of two, namely the *g* ($\lambda_{\text{eff}} = 4770 \text{ \AA}$) and *r* ($\lambda_{\text{eff}} = 6231 \text{ \AA}$) filters. We measured the counts of each galaxy in these SDSS images inside a $30''$ diameter aperture. These counts were converted to flux following the counts-to-magnitude prescription in SDSS documentation⁵. We crosschecked this method measuring magnitudes of stars on each field and comparing them with SDSS DR6 photometric catalogue, obtaining less than 0.05 magnitude dispersion for $g < 17.5$ mag.

We then extracted the spectrophotometry from our reduced cubes, summing the flux of individual spectra inside a $30''$ diameter aperture around the peak intensity of the object, and convolving this spectrum with the SDSS *g* and *r* filter passbands (Jester et al. 2005). Using these two data pairs, a scaling solution of the form:

$$F_{\text{corr}}(\lambda) = F_0(\lambda) \times a \quad (1)$$

was derived for each band, where $F_{\text{corr}}(\lambda)$ and $F_0(\lambda)$ are the re-calibrated and original fluxes, respectively, and a is the calibration constant. The *root-mean-square* (*rms*) for these values is $\sim 4\%$ in the *g* band and $\sim 5\%$. Finally, the average of the two scaling constants derived for the *g* and *r* filters is adopted. In this way we were able to recalibrate the spectrum to match the SDSS photometry.

Figure 4 shows two examples for the resulting re-calibrated spectra observed with the V300 and V600 grating. Together with the values for the *g* and *r* filters used in this re-calibration, we present the derived values for SDSS *u* and *i* bands. In addition to these measurements, the figure includes the fluxes corresponding to the Johnson *B*, *V* and Cousin *R_C* magnitudes determined on the basis of the SDSS photometry and the transformation equations presented by Jester et al. (2005)⁶. There is a good agreement in all cases suggesting that this re-calibration method is reliable.

Figure 5 (top panels) shows the *g* and *r*-band magnitudes derived from the datacubes and the SDSS images before (blue

⁵ <http://www.sdss.org/dr7/algorithms/fluxcal.html#counts2mag>

⁶ Summary of the transformations in <http://www.sdss.org/dr7/algorithms/sdssUBVRITransform.html>.

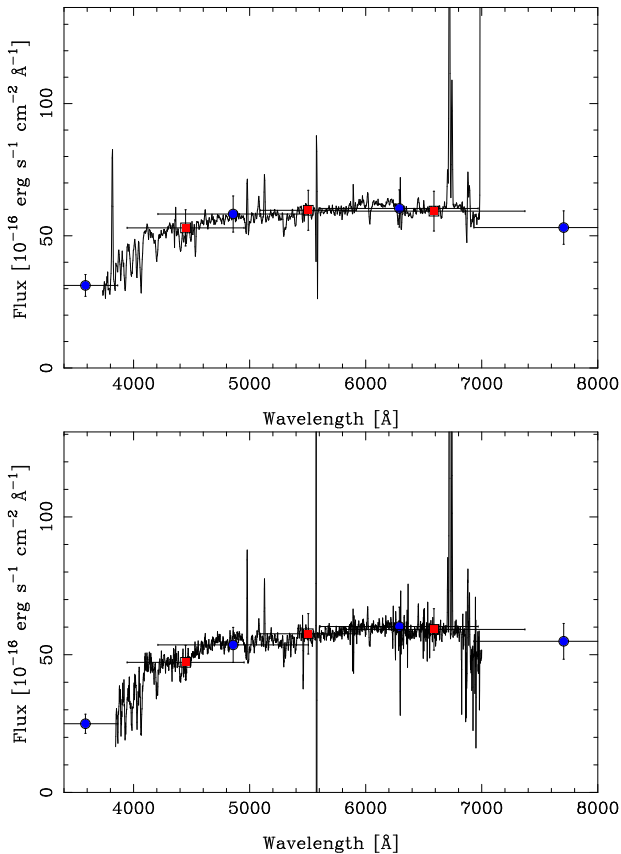


Fig. 4. Examples of the flux re-calibration based on SDSS photometry for CGC071-96 (observed with the V300 grating, *top panel*) and CGCG430-046 (V600 grating, *bottom panel*). The values for the SDSS *g* and *r* filters used in the re-calibration are presented with blue solid circles, as well the derived values for SDSS *u* and *i* filters. Johnson *B*, *V* and Cousins *R_C* magnitudes are also shown (red solid squares) to test the flux calibration.

solid circles) and after (red solid squares) the recalibration process. Both photometric data match for the 85% of the galaxies within a range of ± 0.15 mag before the recalibration (just 4 objects present a higher dispersion below ± 0.25 mag). The possible differences in colours is explored in Fig. 5, bottom panel. Any possible error in the relative flux calibration from blue to red would produce a change in colour. The dispersion (rms) around the one-to-one relation is ~ 0.1 mag, consistent with the expected errors from propagating both the SDSS photometric errors ($\sim 4-5\%$) and the absolute flux calibration accuracy of our data ($\sim 8\%$).

In the few cases (11 targets) when the SDSS photometry is not available for a galaxy, we obtained broad-band images using CAFOS at the 2.2 m telescope of the Calar Alto Observatory, Spain. The observations were carried out for 6 nights from January 28th to March 30th, 2010, when images with the Johnson *B*, *V*, *I*, and Cousins *R_C* filters were obtained. The CCD camera was equipped with a SITE pixel chip. The pixel size was $24 \mu\text{m}$, corresponding to $0.53''$. Sky flats were exposed in every dawn and dusk phase. Bias subtraction, flat-field division, and trimming were performed in the usual manner, using the IRAF package.

We photometrically calibrated these images using GSC2.3 (Lasker et al. 2008) and USNO-B (Monet et al. 2003) catalogues as it follows. We obtained *B* and *V* photometry for our galax-

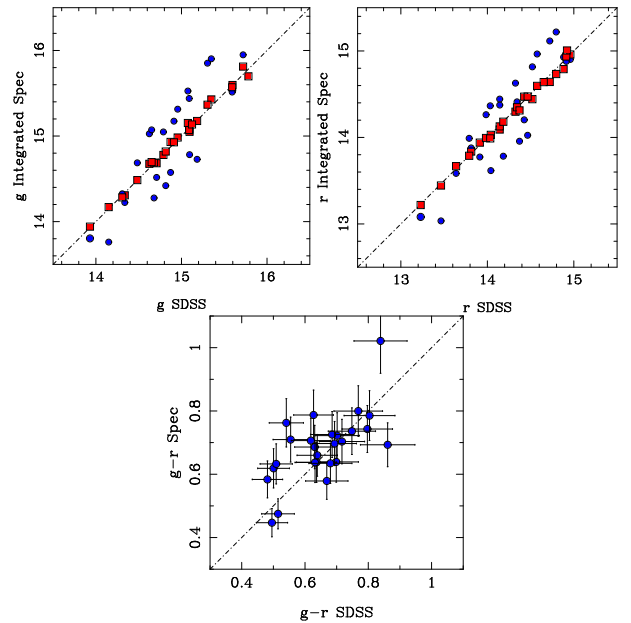


Fig. 5. Top: Comparison of *g* (right panel) and *r*-band (left panel) magnitudes derived from the integrated spectrum within an aperture of $30''$ /diameter extracted from the V600 datacubes and the corresponding magnitudes derived from the SDSS images, before (blue solid circles) and after (red solid squares) the flux calibration described in the text. Bottom: Comparison of *g-r* colour. Considering the errors in the absolute flux calibration ($\sim 8\%$) and between *g* and *r* band (around $4-5\%$), the expected errors in the colours are ~ 0.1 mag, consistent with the errors in SDSS photometric data.

ies using the *qphot* routine of the IRAF and adjusted the zero-point (ZP) magnitude to the GSC2.3 and USNO-B photometry. For these ZP calibration we measured the magnitudes of several stars (7-8) in the same field of our galaxies and then we determined the difference between our magnitudes and the catalogued ones. In general, the dispersion obtained for the ZP determined using the USNO-B catalogue was nearly 0.4 mag on average, so we decided to use the GSC2.3 ZP with a dispersion of 0.2 mag on average. One ZP was calculated for each image with this method. Following the same procedure described before, we then convolved a similar aperture spectra extracted from the datacubes with the *B* and *V* filter responses, obtaining another pair of data sets for recalibrating these cubes. Considering that the stars from the GSC2.3 catalogue used in this work presented errors of $0.1-0.4$ mag, we expect that our recalibration procedure ensures an absolute spectrophotometric calibration better than a $\sim 15\%$ in all the spectral range.

Finally, the pipeline performs a set of quality control measurements, that are accessible to the user on a web-based interface, as indicated above. Among these measurements the most relevant are (i) cross-checks of the focus accuracy of the instrument, (ii) independent estimations of the accuracy of the wavelength calibration (by comparing the nominal wavelength of the most prominent emission lines included in the sampled wavelength range with the measured ones on the data, for each individual spectra within the reduced RSS), (iii) estimations of accuracy of the sky-subtraction (from the residual flux of the strongest and more variable night-sky emission line in the considered wavelength range $-OI 5577 \text{ \AA}$), (iv) estimations of the night-sky brightness at the moment of the observation, (v) esti-

Table 4. Automatic quality control measurements along the pipeline. The average 5σ limit V -band magnitude, the V -band magnitude of the sky and the accuracy of the wavelength calibration are presented for each night.

Observing date	5σ limit V -band (mag)	Sky V -band magnitude	Wavelength calibration (\AA)
2007-06-22	22.73	20.50	0.30
2007-06-23	22.50	20.50	0.30
2009-03-19	23.02	20.25	0.43
2009-03-20	23.02	20.28	0.34
2009-03-21	22.92	20.10	0.26
2009-03-22	22.84	20.12	0.39
2009-03-23	21.54	19.07	0.22
2009-03-24	23.19	19.01	0.32
2009-06-27	23.05	20.13	0.35
2009-06-28	23.75	18.35	0.30
2009-10-17	22.55	20.05	0.15
2009-10-18	21.58	19.42	0.20
2009-10-19	22.00	19.83	0.15
2009-10-22	22.42	20.13	0.15
2009-10-23	22.32	19.73	0.23

mations of the depth of the final datacubes (by computing the signal-to-noise ratio in the spectral range $5670 - 5730 \text{\AA}$). For the observations presented in this paper, the average 5σ detection limit is $\sim 22.5 - 23.0 \text{ mag/arcsec}^2$ (V -band) and the accuracy of the wavelength calibration is $\sim 0.3 \text{\AA}$. In Table 4 we present these values, together the V -band magnitude of the sky, for each observing night. On the basis of these quality control procedures, it is possible to discard seven datacubes due to their poor quality. Most of these objects were observed under non photometric conditions, and the control has clearly identified them to be discarded, as expected.

5. Analysis and results

In order to extract physical properties of the galaxy from the data set, it is necessary to identify the emission lines produced by ionised gas in the galaxies, and decouple this emission from the underlying stellar population. Particular care has to be taken in this decoupling technique, since some of the emission lines (e.g. $H\beta$) may be strongly affected by underlying absorption features. Several authors has developed different fitting codes to obtain information about the stellar content and star formation history of galaxies (e.g., Cid Fernandes et al. 2005; Ocvirk et al. 2006; Sarzi et al. 2006; Koleva et al. 2009; MacArthur et al. 2009). In this paper we adopted the decoupling method proposed by Sánchez et al. (2011b), based in a full spectrum modelling. This method involves a linear combination of multiple stellar populations and the non-linear effects of dust attenuation to obtain information about the ionised gas and the stellar content of the galaxies, and can be applied to each of the individual spectra of the datacubes to obtain the two dimensional distribution of the parameters derived with this procedure.

In this section we present the method (§ 5.1) and analysis of the accuracy of the physical properties derived with this method (§ 5.2). We present in § 5.3 a comparison with the SDSS data, and we explore differences in the properties derived from two different aperture obtained from the data in § 5.4. Finally, a first analysis from the two dimensional spectroscopic data is presented (§ 5.5).

5.1. Decoupling the stellar population and gas content

The method for the decoupling of the stellar populations from the emission lines can be summarised as follows (for a more detailed description, see Sánchez et al. 2011b): (i) A set of detected emission lines was identified in the spectrum. (ii) The underlying stellar population was fitted by a linear combination of a simple grid of six single-stellar populations (SSPs) templates by Vazdekis et al. (2010), with three ages (0.089, 1.000 and 17.7828 Gyrs) and two metallicities ($Z = 0.0004$ and 0.03)⁷. These templates were first corrected for the appropriate systemic velocity and velocity dispersion (including the instrumental dispersion), taking into account the dust attenuation⁸. In addition, a spectral region of 30\AA width around each detected emission line was masked prior to the linear fitting, including also the regions around bright sky-lines (Sánchez et al. 2007a). (iii) Once we derived a first approximation of the spectrum of the underlying stellar population, this was subtracted from the original spectrum to obtain a pure emission-line spectrum. (iv) To derive the intensity of each detected emission line, this emission-lines spectrum was fitted to a single Gaussian function per emission line plus a low order polynomial function for the local continuum. (v) A pure gas-emission spectrum was created, based on the results of the last fitting procedure, using only the combination of Gaussian functions. The pure gas-emission model was then subtracted from the original spectrum to produce a spectrum of gas-free spectra. (vi) This spectrum is fitted again by a combination of SSPs, as described before (but without masking the spectral range around the emission lines, in this case), deriving the luminosity-weighted age, metallicity and dust content of the composite stellar population. (vii) Finally, individual emission-line fluxes are measured in each spectrum by considering spectral window regions around the most prominent emission lines (fitting of Gaussian functions to $[\text{O II}]\lambda 3727$, $H\beta$, $[\text{O III}]\lambda\lambda 4959, 5007$, $H\alpha$, $[\text{N II}]\lambda 6548, 83$, $[\text{S II}]\lambda\lambda 6717, 6731$). With this method, we obtain information about the ionised gas and the stellar content in the analysed spectrum.

This decoupling method can be applied to any galaxy spectrum, either integrated spectrum or individual spectra in the datacubes, to analyse the spatially resolved spectroscopic properties. As an example, we show in Fig. 6 the best fitted gas-emission (red line) and stellar population (green line) spectra obtained when applying this decoupling method on the central spectrum of CGC071-096 galaxy (black line). The differences between the real spectrum and the final fitting are shown with a blue line. These residuals represent an error of $\sim 7\%$ over the signal of the global spectrum, and it shows the good agreement of the global fitting.

5.1.1. Star formation history

To explore a more realistic interpretation of the computed stellar population, we decided to compare the galaxy data not only with SSPs, but also with spectra obtained from a given star formation history (SFH). With this aim, we used the population synthesis models by Vazdekis et al. (2010). These models provide the time (T) evolution of the synthesised spectra of galaxies characterised by an initial metallicity (Z), a star formation history (SFH) and

⁷ This grid of templates has been also adopted by Viironen et al. (2011) in their analysis of UGC9837 galaxy from this data set.

⁸ The dust attenuation is also a free parameter in this decoupling method. The extinction law of Cardelli et al. (1989) is adopted, with a ratio of total to selective attenuation $R_V = 3.1$ (Jenkins 1987).

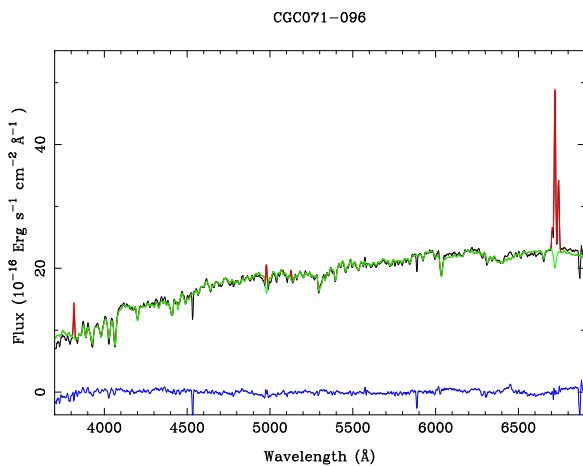


Fig. 6. Example of the decoupling of emission lines and underlying stellar population for CGC071-096. We show the central spectrum in black line, the best-fit model for the emission lines in red, and the best fitted stellar population, modelled as a linear combination of different SSPs, plus the computed dust extinction, in green. Finally, the differences between the real spectrum and the final fitting is shown in blue.

an initial mass function (IMF) ($F_{\lambda}(T)[Z, SFH, IMF]$). We considered an pure exponential-declining SFH (Sandage 1986):

$$\text{SFR}(t) = \exp(-(T_0 - t)/\tau) \quad (2)$$

where the steepness of the decay are regulated by a single parameter τ . To obtain the final spectra we considered a simple (not delayed) exponential, being $T_0 = 15.5$ Gyr the age of the galaxy today, and a Salpeter IMF (a unimodal IMF with $\mu = 1.3$). With these input data and using the tools provided in the MILES (Medium-resolution Isaac Newton Telescope library of empirical spectra) website⁹, we created a grid of spectra with solar and sub-solar metallicities ($Z = 0.019, 0.0004$) and τ from 1 to 19 in steps of 2 Gyr, with a S/N ~ 50 per pixel in the continuum, and spectral resolutions corresponding to the V300 and V600 grism.

In order to obtain the equivalence between the characteristic time scale parameter τ and the stellar population parameters, i.e., luminosity-weighted age and metallicity, we applied the fitting procedure explained in the previous section, using as input the spectra generated from these SFHs. In Fig. 7 we represent the luminosity-weighted age and metallicity derived for the grid of spectra from the different SFH parametrised by τ as a function of this parameter. As it can be seen, we obtain a clear dichotomy for the metallicity. This is expected since we are considering two different metallicities for the spectra created from a given SFH. In this sense, the metallicity is well recovered for all the values of τ , although the metallicity is over-estimated in the case of the solar metallicity due mainly to the limited available values in the grid of models using in this experiment.

In the case of the age, we obtain old stellar ages for low values of τ and younger ages until $\tau > 10$, where the age becomes almost constant. This agrees with Gavazzi et al. (2002), who found that dwarf and normal elliptical galaxies, i.e. galaxies with older stellar populations, are well characterised by $\tau \leq 3$. They also found that galaxies with younger stellar populations present $\tau \geq 4$, as spiral galaxies (Sa-Sb) with values of $4 < \tau < 6$, and blue compact dwarfs with $\tau \geq 7$. The equivalences obtained here

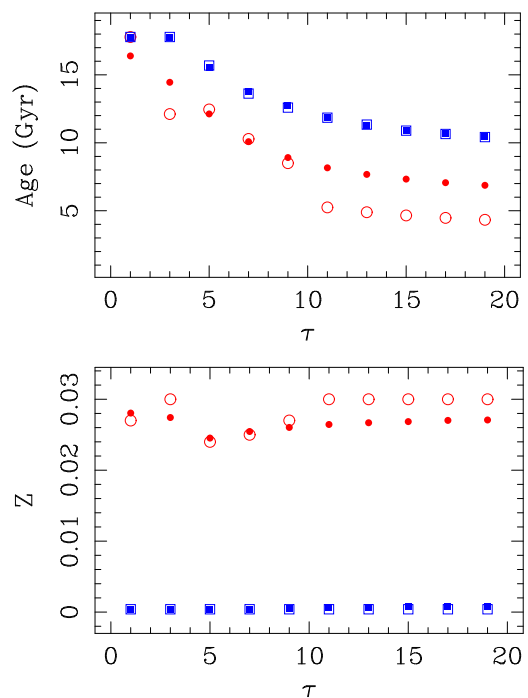


Fig. 7. Equivalence between the stellar population parameters, i.e the luminosity-weighted age (top panel) and the luminosity-weighted metallicity (bottom panel), and the characteristic time scale parameter τ for the two SFH considered (red circle for solar metallicity, blue squares for sub-solar). We present the results of the fitting procedure applied to mock galaxies with the V600 resolution, when the dust attenuation is fixed (filled symbols) and computed (open symbols).

(Fig. 7) will be used for a characterisation of the stellar populations in § 5.2.4.

5.2. Accuracy of the derived properties

Following the idea of recent works based on IFU observations, (e.g., Bershady et al. 2010b; Sánchez et al. 2011b), we explore in this section the accuracy in the measurements of different parameters of our interest (e.g., emission line fluxes, redshift, velocity dispersion, dust extinction, average stellar populations). With this aim, we created a set of mock spectra of galaxies with different kinematic galactic parameters (velocity dispersion, redshift), underlying stellar populations (old or young SSP), ionised gas and signal-to-noise (S/N) in the continuum. These mock spectra were generated as follows. First, we consider an underlying stellar population using the stellar population models provided by Vazdekis et al. (2010)¹⁰. We consider four possibilities for the underlying stellar population: a single stellar population (young -0.7 Gyr and solar metallicity ($Z = 0.019$) – or old -12.6 Gyr and metallicity of $Z = 0.004$), or two stellar populations mixed in different ratios (10% of young plus 90% of old stellar population -2SSP-10-, and 1% of young plus 99% of old stellar population -2SSP-01). Next, we add an emission-line spectrum to simulate the ionised gas in the mock galaxy. To obtain more realistic data, we measured the emission lines on several regions of NGC628 from the 2D spectroscopic data presented by Sánchez et al. (2011b), and we scaled these values to obtain similar values than the ones measured in a real galaxy of

⁹ <http://www.iac.es/proyecto/miles/pages/webtools/get-spectra-for-our-files>, <http://www.iac.es/proyecto/miles/>

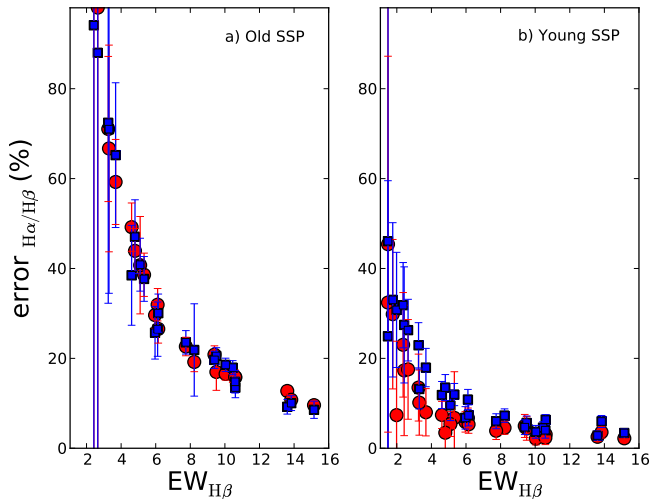


Fig. 8. Relative errors in the $H\alpha/H\beta$ ratio when the dust attenuation is fitted (blue squares) or fixed (red circle) for different equivalent width of the $H\beta$ emission line ($EW_{H\beta}$), for a spectrum of a mock galaxy with a pure old (left panel) or young underlying stellar population (as explained in the text).

our sample (see e.g. Viironen et al. 2011). The nebular continuum is considered negligible. Then we apply different values of dust attenuation, same for the stellar continuum and the emission lines. Next, we consider the kinematics of the mock galaxy, i.e., we broaden the spectrum to a given velocity dispersion σ and shift it to a given redshift z . Finally, we add noise to the spectrum to simulate a real galaxy observation. As result of this process, we obtain a spectrum of a mock galaxy with well-known parameters that we can change to check the recovering of the information for these studies.

In next sections we present the different studies that we have carried out to analyse the accuracy in measurements of the dust attenuation (§ 5.2.1), kinematics (§ 5.2.2), ionised gas (§ 5.2.3), and underlying stellar population (§ 5.2.4), of the galaxies observed with the two setups (V300 and V600) used in this work.

5.2.1. Dust attenuation

The treatment of the dust attenuation may affect the resulting derived parameters of the stellar population (i.e., the luminosity-weighted age and metallicity, Calzetti 2001; Muñoz-Mateos et al. 2007, 2009). As part of the decoupling method explained above, we adopted the Cardelli et al. (1989) law, which may be not the optimal solution to study the dust attenuation in star-forming galaxies (e.g., Calzetti 2001). Recently, MacArthur et al. (2009) considered the attenuation law based on the two component dust models by Charlot & Fall (2000), especially developed for star-formation galaxies. Despite the conceptual differences between these attenuation laws, both of them present a very similar shape in the wavelength range of our data, and it is not wide enough to distinguish between these different laws.

To explore the impact of fitting the dust attenuation on the derived parameters, we generated a set of mock spectra of galaxies following the procedure explained above. Since values of equivalent widths of the $H\beta$ emission line $EW_{H\beta} > 3.5 \text{ \AA}$ are suitable to perform an abundance analysis in galaxies despite the

dependence on other physical properties of the ionising cluster (e.g., its age), we decided to explore a range of equivalent widths of $EW_{H\beta} \sim 1.5 - 15 \text{ \AA}$ for our mock galaxies. Then we applied the fitting technique (i) fixing the value for the dust attenuation, or (ii) computing A_V with the fitting program, with values of A_V varying between $A_V = 0.1$ and 1.2 , in steps of 0.1 .

We present the results of this experiment in Fig. 8, where we show the relative random errors obtained for the $H\alpha/H\beta$ ratio (in absolute values) when the dust attenuation fixed (red circles) and fitted (blue squares), as a function of $EW_{H\beta}$. In all cases, the $H\alpha/H\beta$ ratio is recovered with a relative error $< 20 \%$ for $EW_{H\beta} > 8 \text{ \AA}$ for an old underlying stellar population (left panel), while the relative errors for a young stellar population is $< 20 \%$ for $EW_{H\beta} > 3.5 \text{ \AA}$ (right panel). Although there are not differences in the determination of $H\alpha/H\beta$ for an old population depending on the method (fitting or not the dust attenuation), slightly higher errors are found when the dust attenuation is fitted in the case of a young underlying stellar population (right panel in Fig. 8). This is due to the effect of the dust attenuation, more important for bluer wavelengths where stronger Balmer absorption lines are found, especially for young stellar populations. In this case, slightly variations in the dust attenuation determination can produce the differences in the $H\alpha/H\beta$ ratio, more evident for small equivalent widths of $H\beta$. We see in Fig. 8 that, in general, the relative errors in the determination of the $H\alpha/H\beta$ ratio are similar regardless the dust attenuation fitting, and then, the accuracy in the determination of the gas content is not depending on the procedure applied.

5.2.2. Kinematics

One of the advantages of using IFU data is the possibility to analyse spatially resolved properties of the galaxies. In particular, kinematic studies can reveal substructures in galaxies such as kinematically decoupled cores in the stellar velocity field and twists in the gas velocity field, and also more hidden substructures as disks and bars. The instrumental setups used in these observations, although limited in spectral resolution, allow some studies of this kind. Data obtained with V300 and V600 grism allow the measurement of redshifts, while the resolution of the V600 grism ($\text{FWHM} = 5.4 \text{ \AA}$) will allow measurements of velocity dispersion above $\sim 140 \text{ km s}^{-1}$. In order to assess the accuracy in the measurements of redshift and velocity dispersion for these observing setups, we applied the fitting method explained above to a set of mock spectra from single stellar populations (an old and a young SSP), and $\text{S/N} = 50$ (per pix) in the continuum. In this case, we considered our mock spectra of galaxies at different redshifts (from 0.015 to 0.025, in steps of 0.001) and they were broadened to different velocity dispersions (from 150 to 350 km s^{-1} , in steps of 25 km s^{-1}). We applied the decoupling method in the spectral range $\lambda\lambda 3950 - 4600 \text{ \AA}$, which comprises clear absorption features suited for this study. In addition, due to the short wavelength considered in this experiment, a fixed value for the dust attenuation was considered, and then, it is not fitted in this case. Finally, for an estimation of the random error in these measurements, we simulated a grid of spectra of each mock galaxy as follows. An average *rms* of the mock galaxy in areas free of sky lines, and galactic emission, or absorption lines was calculated and added by bootstrapping method to the SSP+gas model spectrum. This was repeated 100 times, and the fitting was done then on the resulting spectra. The results are presented in Fig. 9, where we show the median relative errors obtained for the velocity dispersion and the redshift

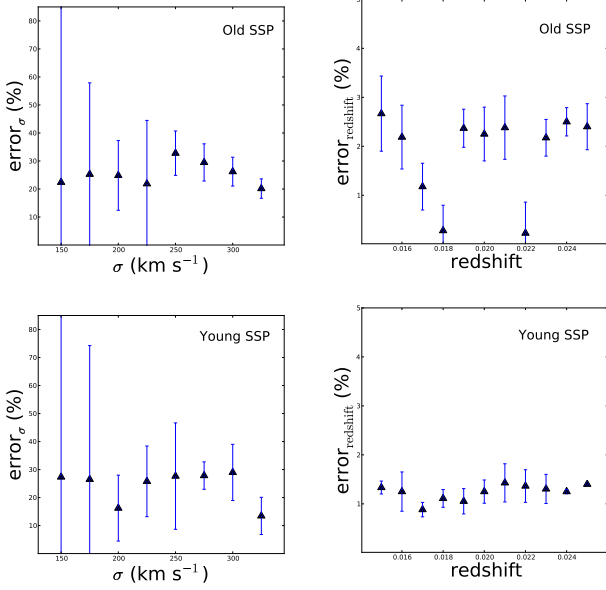


Fig. 9. Estimated relative random errors in the measurements of velocity dispersion (left panels) and redshift (right panels) for mock galaxies with an old (upper panels) and young (lower panels) underlying single stellar populations, as explained in the text, for observations with the medium resolution grism (V600).

for each mock galaxy. The error bars represent the standard deviation computed from the simulations. We find that for both underlying stellar populations, we recover the redshifts with errors $< 5\%$. As expected, the relative errors in determination of the velocity dispersion are high for values close to the instrumental setups. It is possible to measure velocity dispersion with a relative error of $\sim 30\%$ for $\sigma > 200 \text{ km s}^{-1}$ (i.e., intrinsic values of the velocity dispersion of galaxies above 140 km s^{-1}).

5.2.3. Ionised Gas

The Integral Field Spectroscopy allows the study of the resolved physical properties of the ionised gas in galaxies, such as (i) local nebular reddening estimates based on the Balmer decrement; (ii) the oxygen abundance distributions based on a suite of strong line diagnostics incorporating reddening-corrected line ratios (e.g., $\text{H}\alpha$, $\text{H}\beta$, $[\text{O II}]$, $[\text{O III}]$, $[\text{N II}]$, and $[\text{S II}]$); and (iii) measurements of ionisation structure in H II regions and diffuse ionised gas using the well-known and most updated forbidden-line diagnostics in the oxygen and nitrogen lines. For all these studies, it is necessary measurements of the fluxes of the emission lines in the individual spectra. To test the accuracy in measured fluxes for the ionised gas, we followed the procedure explained above to create a set of mock galaxies at redshift $z = 0.02$ with a velocity dispersion $\sigma = 150 \text{ km s}^{-1}$ and $\text{S/N} = 50$ (per pix) in the continuum. We measured the main emission lines (see § 5.1) in 29 different regions in NGC628, and we created 29 spectra with gaussians of these values. In this way, the emission line ratios of the mock galaxies are realistic and known in advance. Then we have applied the decoupling method and measured the emission line fluxes. Finally, we have compared these results with the input data from NGC628. In Fig. 10 we plot the relative random error of the ratio of $\text{H}\alpha/\text{H}\beta$ as a function of the equivalent width for the $\text{H}\beta$ emission line. We obtain relative errors of the ratio of $\text{H}\alpha/\text{H}\beta < 10\%$ when $\text{EW}_{\text{H}\beta} > 5 \text{ \AA}$

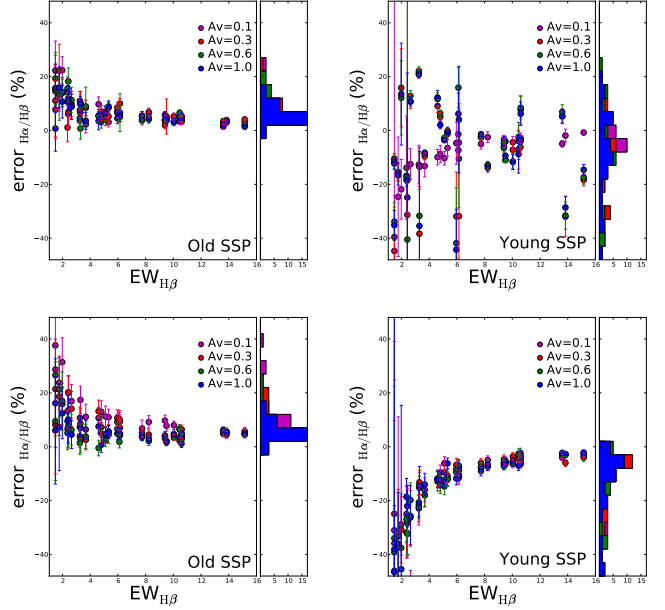


Fig. 10. Study of the recovering of the properties of the ionised gas for the observations with the medium resolution grism (V600). Estimated relative random errors in the measurements of the $\text{H}\alpha/\text{H}\beta$ ratio as a function of the equivalent width of $\text{H}\beta$ emission lines ($\text{EW}_{\text{H}\beta}$) on mock galaxies with an old (left panels) and a young (right panels) underlying stellar population and different values for the dust attenuation: magenta for $A_V = 0.1$, red for $A_V = 0.3$, green for $A_V = 0.6$ and blue for $A_V = 1.0$. Top panels are for dust attenuation fixed in the program, and bottom panels for dust attenuation fitted in the program. Each block of the histogram represents an error of 5%.

for old stellar populations, while we obtain errors of $< 20\%$ always that $\text{EW}_{\text{H}\beta} > 6 \text{ \AA}$ for young stellar populations. There is a tendency to over-estimate the emission of $\text{H}\beta$ for old stellar populations (left panels), while we find the opposite behaviour for young stellar populations (right panels). This is expected since the Balmer absorption lines are deeper for a young stellar population and an accurate decoupling is more difficult if the emission lines are not very intense. In addition, this effect is clearer when the dust attenuation is also fitted in the decoupling method (lower panel in Fig. 10).

5.2.4. Stellar Populations

As explained before, the decoupling method also provides with the best combination of stellar populations to reproduce the underlying stellar population of galaxies. In this section we study the recovering of the luminosity-weighted age and metallicity from the data obtained in this work. With this purpose, we applied the decoupling method on spectra of mock galaxies with different underlying stellar populations and gas content (see § 5.2), at redshift $z = 0.02$ with a velocity dispersion $\sigma = 150 \text{ km s}^{-1}$. We considered different S/N ($= 5, 10, 25, 50, 80, 100$ per pixel) in the continuum of the spectra. In addition, we created a grid of spectra from each mock galaxies for error analysis, following the procedure explained in previous sections. Then, we applied the decoupling method in two cases: (i) the dust attenuation is a well known and fixed value (results for the luminosity-weighted age in Fig. 11), and (ii) the dust attenuation is a free parameter in the fitting procedure (results

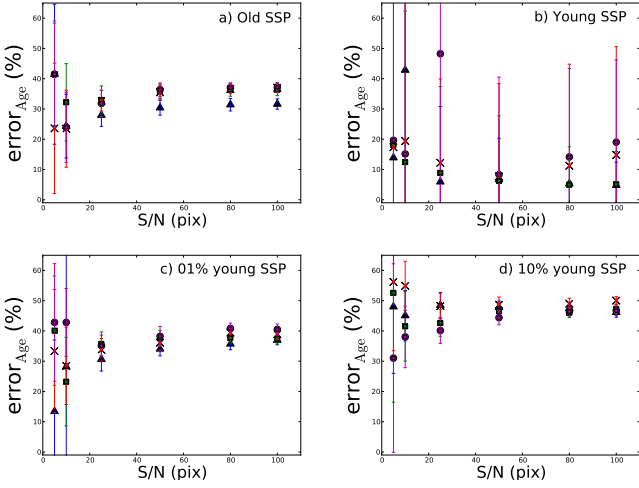


Fig. 11. Study of the recovering of the luminosity-weighted age as a function of the S/N in the continuum for the V600 grid. In this case, the dust attenuation has been considered known and fixed when applying the decoupling method. Different colours are used for different values of $H\beta$ emission line.

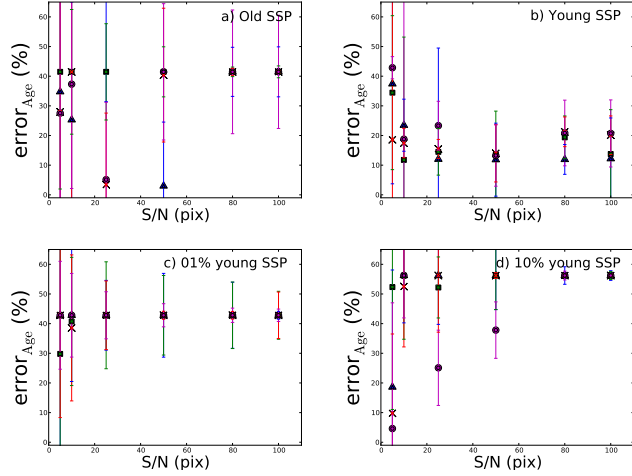


Fig. 12. Same figure than Fig. 11 when the dust attenuation is also computed with the decoupling method. In this case, the estimated random errors (and their standard deviations) are significantly higher than in the previous example.

in Fig. 12). In both cases, we represent the relative error in the luminosity-weighted age for the four cases of underlying stellar population. The error bars show the standard deviation for these values computed from 100 simulations, as in previous sections.

As it can be seen, the relative random errors in the luminosity-weighted age for mainly old stellar populations (panels *a*, *c* and *d* in Figs. 11 and 12) are $\sim 30 - 55\%$ while the estimated errors and their standard deviation are higher, in average, when considering younger stellar populations (panel *b*). In addition, the relative errors are significantly higher in the case of fitting simultaneously the dust attenuation (Fig. 12). It is clear from this analysis that the spectral range (similar for data obtained with V300 and V600 grids) is not wide enough to break the age-metallicity-dust degeneracy. Additional information in other spectral bands, as ultraviolet and infrared, are desirable in order to obtain a reliable value for an independent estimate of the dust attenuation. In that case, dust attenuation would be fixed to

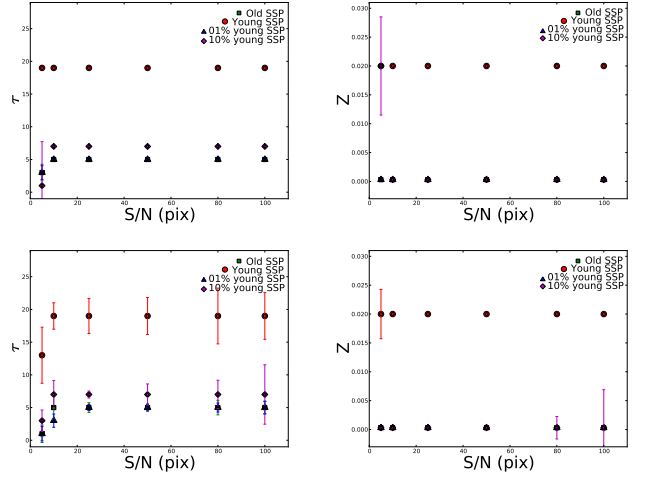


Fig. 13. Parameters of the most similar SFH spectra (τ -left panels- and metallicity -right panels) obtained with the decoupling method, as a function of the S/N in the continuum for the V600 grid. In this case, the dust attenuation has been considered known and fixed in the top panels. Results when the dust attenuation has been fitted are presented in the bottom panels. Symbols and colours are used for different underlying stellar populations of the mock galaxies, as it is indicated in the label.

this value in the fitting process and a more accurate determination of the rest of parameters will be obtained.

In addition, the relative random errors in the luminosity-weighted metallicity are extremely high, above the 100% in all the cases. This indicates that the grid of templates, based in six stellar population models, are too simple for the estimate of metallicity. As noted by MacArthur et al. (2009) and showed by Sánchez et al. (2011b), the analysis of the stellar populations is limited by the templates used. Tentative tests with a grid of 20 and 25 SSPs decrease the error in the luminosity-weighted metallicity to $\sim 35\%$, and therefore a study of the stellar populations is possible with this data by assuming the long computational time necessary. It is important to highlight, in any case, that the recovering of the kinematics and the properties of the ionised gas are well performed with the simple grid considered in this paper, and a further analysis of the stellar population parameters is feasible with an appropriate grid of templates.

Due to the uncertainties obtained in the luminosity-weighted age and metallicity when a grid of SSPs is considered in the decoupling method, we decided to compare our mock galaxies with spectra obtained from a given SFH (see § 5.1.1). As part of the fitting procedure explained in § 5.1, there is an additional option to compute the most similar spectrum to the input one from a collection of spectra. This option is independent of the global fitting to decouple the ionised gas and the stellar population, and we can feed the procedure with a different set of template spectra for this experiment. We used this option to explore which SFH spectra (§ 5.1.1) is more appropriate to describe our mock galaxies. In Fig. 13 we represent the τ parameter (left panels) and metallicity (right panels) for these mock galaxies, when the dust attenuation is fixed (upper panels) or fitted (lower panels). The results in both cases are similar, obtaining low values of τ ($4 < \tau < 6$) for predominantly old stellar populations and a high value ($\tau \sim 20$) for younger stellar populations. In both cases, the metallicity is well determined, as expected since we consider two metallicity values for this experiment (see § 5.1.1).

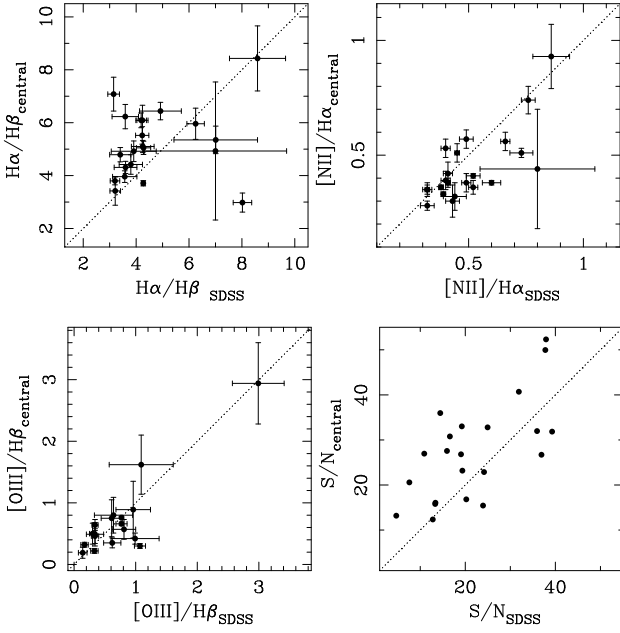


Fig. 14. Comparison of the $H\alpha/H\beta$, $[N\text{II}]\lambda 6583/H\alpha$ and $[O\text{III}]\lambda 5007/H\beta$ ratios, derived from central spectra for the galaxies in this sample and the SDSS spectral, using the multi-SSP fitting procedure, plus the comparison between the S/N in both spectra.

5.3. Comparison with the SDSS data

There are 28 galaxies observed in the sample with available SDSS spectroscopy (marked in Table 1). In order to compare the quality of both data sets, we extracted an integrated spectrum inside a circular aperture of $5''$ from the datacubes, centred in the intensity peak of the galaxy at the V-band. The extracted aperture is selected to match the aperture of the SDSS fibers, taking into account possible errors in the centroid accuracy and seeing effects in the SDSS observations, and the dithering scheme adopted in this work. Then we applied the decoupling method to the spectra of both samples, deriving their physical properties. A full comparison is shown in Fig. 14. Four of the galaxies from SDSS present $S/N < 10.0$ (per pixel, computed over the full spectra), while just one of the galaxies in our sample are below this level. As expected, there is a good agreement between the values from both samples, especially for the stronger, clearly de-blended emission lines, as $[O\text{III}]\lambda 5007/H\beta$ (determination coefficient for a least squares fits to the data $r^2 = 0.79$). For those galaxies with different measurements, it is possible that the SDSS fiber would not be well centred in the galaxy, and we are just comparing different regions of the galaxy. In addition, the S/N of the galaxies observed in this work is higher in average than the presented for the SDSS data.

5.4. Aperture effects in spectroscopy

One of the advantages of Integral Field Spectroscopy is the possibility of integrating different combinations of the observed spectra for particular studies. For example, Rosales-Ortega et al. (2010) analysed aperture selected spectra of individual H II regions within the galaxies of the PINGS survey, and Sánchez et al. (2011b) (and Viironen et al. 2011) explored the aperture effects in the galaxies of this survey, using the IFU as a large aperture spectrograph.

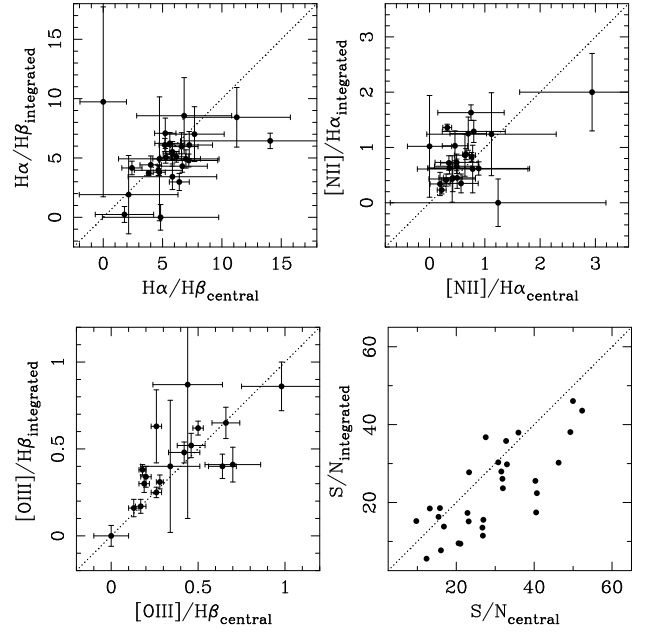


Fig. 16. Same as in Fig. 14 for the comparison of the values derived from central and integrated spectra for the galaxies in this sample.

In this section, we analyse two aperture spectra derived for each galaxy in the sample: a central spectrum, obtained as explained in the previous section, and a $30''$ diameter aperture spectrum, which comprises most of the observed regions of each galaxy above the 5σ detection limit. This spectrum is a good representation of the integrated properties of each galaxy. In Fig. 15 we present both aperture spectra for the subset of galaxies in Fig. 1. As it can be seen, the integrated spectra present stronger emission lines than the central ones, as expected since they are covering also the external parts and different structures of galaxies with usually more amount of ionized gas. There are also differences in the stellar continuum of both apertures for some of the galaxies, with redder colours in the central spectra than in the integrated one, which point to older stellar populations in the central part of the galaxies. For a further comparison, we applied the fitting technique presented above to both spectra, deriving the main properties for the galaxies in the sample. We represent the values derived from both spectra in Fig. 16 for the main emission line ratios. Again, it can be seen differences between both measurements, as expected since they are integrating different regions in the galaxies. In particular, the central aperture is mainly dominated by the bulge of galaxies, where little ionised gas is usually found. On the other hand, the integrated aperture covers the most of the galaxy size and includes arms, bars, and other structures in the galaxies with different gas and stellar content.

As an example of the impact of the differences obtained when analysing both spectra, in Fig. 17 we present the classic diagnostic diagram for emission lines galaxies (e.g., Veilleux & Osterbrock 1987), using the $[O\text{III}]\lambda 5007/H\beta$ and $[N\text{II}]\lambda 6583/H\alpha$ ratios from central (blue filled squares) and integrated (green filled circles) spectra. The Kauffmann et al. (2003) (blue dashed line) and Kewley et al. (2001) (red solid line) demarcation curves usually invoked to distinguish between star forming and AGN galaxies, respectively, are also plotted. For the integrated spectra, 34 of 46 galaxies (i.e., 73.91 % of the sample) present accurate emission line ratios (with an error of

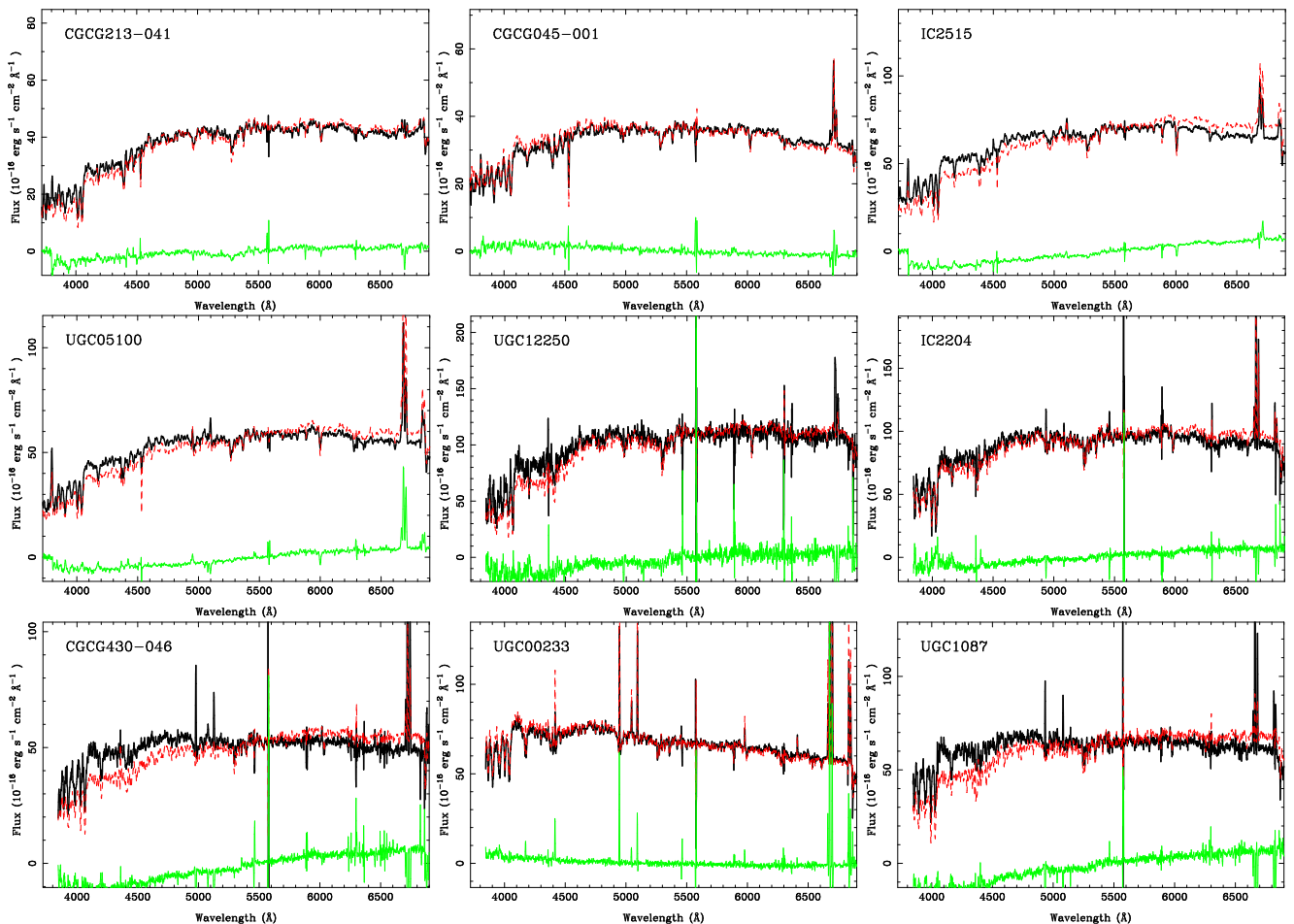


Fig. 15. Comparison of the central (red) and the integrated (black) spectra for the subset of galaxies presented in Fig. 1, normalized to the flux of the central spectrum at 5000 – 6000Å. Differences between both spectra are plotted in green.

$< 30\%$). With these data it is found that 30 galaxies are classified as pure star forming galaxies (88.23 % of the galaxies with accurate emission line ratios), 4 galaxies are in intermediate region (11.76 %) and there are no AGN candidates. 2 galaxies in the sample show little gas ($F_{H\alpha} < 0.1 \cdot 10^{-16}$ cgs Units). Based on the properties of the central spectra, just 25 (of 46) galaxies present accurate emission line ratios (i.e., 54.35 % of the sample), 14 of them are classified as star forming galaxies (56.00%), 2 galaxies (8.00%) are AGN candidates: IC 2515, classified as Sy2 in the BAT catalogue¹¹ (Cusumano et al. 2010), and CGCG 428-059, galaxy already detected in radio and X-rays (Hardcastle et al. 2007), what indicates that probably hosts an AGN. There are 9 galaxies in the intermediate region (36.00%). In particular, 2MASX J13062093+5318232, classified as AGN in NED database (see Table 1, appears in the intermediate region, but the error in the $[N\text{II}]\lambda 6583/H\alpha$ ratio is $> 30\%$ and it will be compatible with its classification as AGN. Finally, in this case 18 galaxies show little gas in their central spectra.

It is clear from this comparison that important differences are found when analysing and comparing spectra extracted with different apertures over a galaxy. The two dimensional data from IFS surveys can be used to analyse these aperture effects (e.g., Viironen et al. 2011), which could be critical for the comparison and interpretation of galaxies at different redshifts. A large number of observed objects using this technique will al-

low to obtain empirical calibrations to compare in an appropriate way the values obtained in the Local Universe with galaxies at higher redshifts.

5.5. Spatially resolved properties

The main advantage of using IFS for the study of galaxies is the ability to derive spatially resolved spectroscopic properties (e.g., de Zeeuw et al. 2002; Rosales-Ortega et al. 2010; Blanc et al. 2010; Castillo-Morales et al. 2010). Using IFS, we obtain a spectrum for each position of the galaxy, and therefore the decoupling method explained before can be applied for each of the individual spectra within the obtained datacubes with enough signal-to-noise. In this way, we obtain two-dimensional distributions (or maps) of the parameters derived by this analysis. Although it is out of the scope of this article to analyse in detail each of them, we present here a few examples to show the quality of the derived maps, focused in this case on the properties of the ionised gas.

Figure 18 shows the two dimensional distribution of the $[N\text{II}]\lambda 6583/H\alpha$ line ratio derived from the fitting procedures described in the text for the sub-set of galaxies in Fig. 1. The blue dashed contours shows the continuum intensity at the R_C - band. The black solid contours shows the $H\alpha$ observed intensity, starting at $0.3 \cdot 10^{-16}$ erg s^{-1} cm^{-2} . Notice that the data presented in this work enable us to reach sensitivity lim-

¹¹ <http://www.pa.iasf.cnr.it/cgi-bin/bat/main/fonti.cgi>

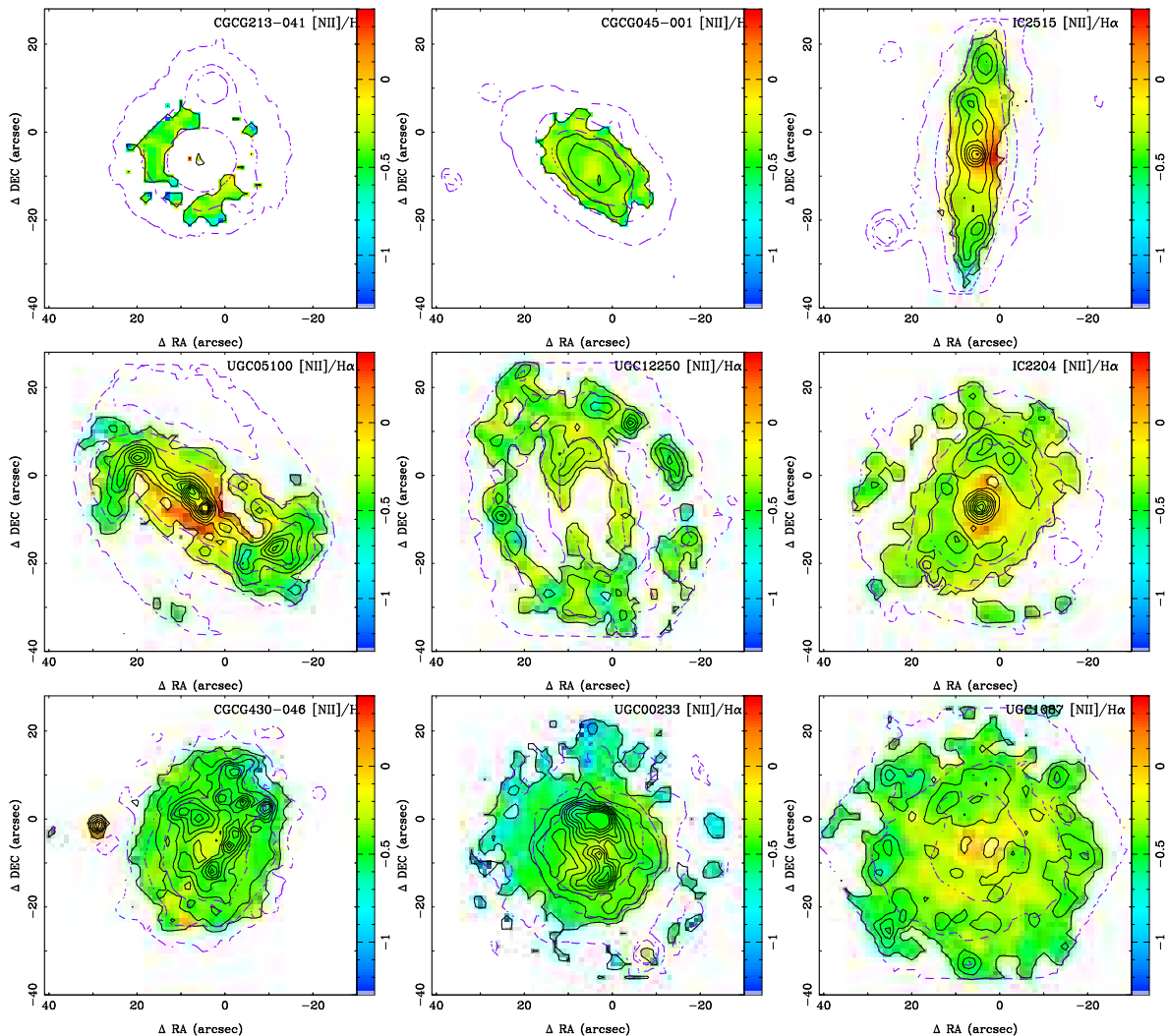


Fig. 18. Colour map of the $[\text{N II}]\lambda 6583/\text{H}\alpha$ line ratio derived from the fitting procedures described in the text, for a sub-set of the observed galaxies. The black solid contours shows the $\text{H}\alpha$ observed intensity, starting at $0.3 \cdot 10^{-16} \text{ erg s}^{-1} \text{ cm}^{-2}$, and with a step of $1 \cdot 10^{-16} \text{ erg s}^{-1} \text{ cm}^{-2}$ for each contour. The blue dashed contours shows the continuum intensity at the R_C - band, starting at $0.03 \cdot 10^{-16} \text{ erg s}^{-1} \text{ cm}^{-2}$, with a step of $0.1 \cdot 10^{-16} \text{ erg s}^{-1} \text{ cm}^{-2}$ for each contour.

its of $\sim 10^{-16} \text{ erg s}^{-1} \text{ cm}^{-2}$, fainter than previous imaging surveys in the Local Universe (e.g. Pérez-González et al. 2003; Helmboldt et al. 2004; Meurer et al. 2006; Kennicutt et al. 2008; Karachentsev & Kaisin 2010), what will allow a more accurate determination of the SFR in the Local Universe. In addition, we present in Fig. 19 the velocity map of the ionised gas (from the $\text{H}\alpha$ emission), derived with the previously described procedure. In most of cases it is seen a clear rotational pattern, mostly due to the bias towards late-type galaxies in the presented sub-set.

Finally, Fig. 20 shows the rotational curves along the kinematic major axis, derived from the velocity maps of $\text{H}\alpha$ (Fig. 19). The colour code indicates the $[\text{N II}]\lambda 6583/\text{H}\alpha$ line ratio presented in Fig. 18. Values for R_{25} are taken from the RC3 catalogue (see Table 1). From the sub-sample shown in Fig. 20, we can see that it is possible a two dimensional study up to $\sim 1.0 R_{25}$ with the data presented in this work, although in most of cases we do not reach so large extension. This easy experiment shows the importance of the sample selection to accommodate the galaxies in the FOV of the PPAK instrument. Closer galaxies with high angular sizes will reach R_{25} out of the FOV, while the S/N of small (and faint) galaxies will be not enough for most of two dimensional studies. This work shows, there-

fore, the importance of the sample selection not only in volume and limit magnitude, but also in the apparent size of galaxies as previous works showed (e.g., Bershady et al. 2010a).

These figures illustrate how suitable is the considered experimental setup for the study of these spectroscopic properties within the full optical extension of the considered galaxies (characterised by the continuum emission). A detailed analysis of the resolved properties of these galaxies will be presented in forthcoming papers.

6. Summary and Conclusions

We present in this paper a IFS study of nearby galaxies, exploiting the capabilities of the wide-field PPAK IFU of the PMAS spectrograph mounted on the 3.5 m telescope. In particular, we explore the requirements to perform a detailed study of the most relevant spatially resolved spectroscopic properties of galaxies in the Local Universe along all their optical extension, focused on: (i) The main properties of the ionised gas; (ii) The luminosity-weighted age and metallicity of the stellar population; (iii) The main kinematic properties of both the ionised gas and stellar population.

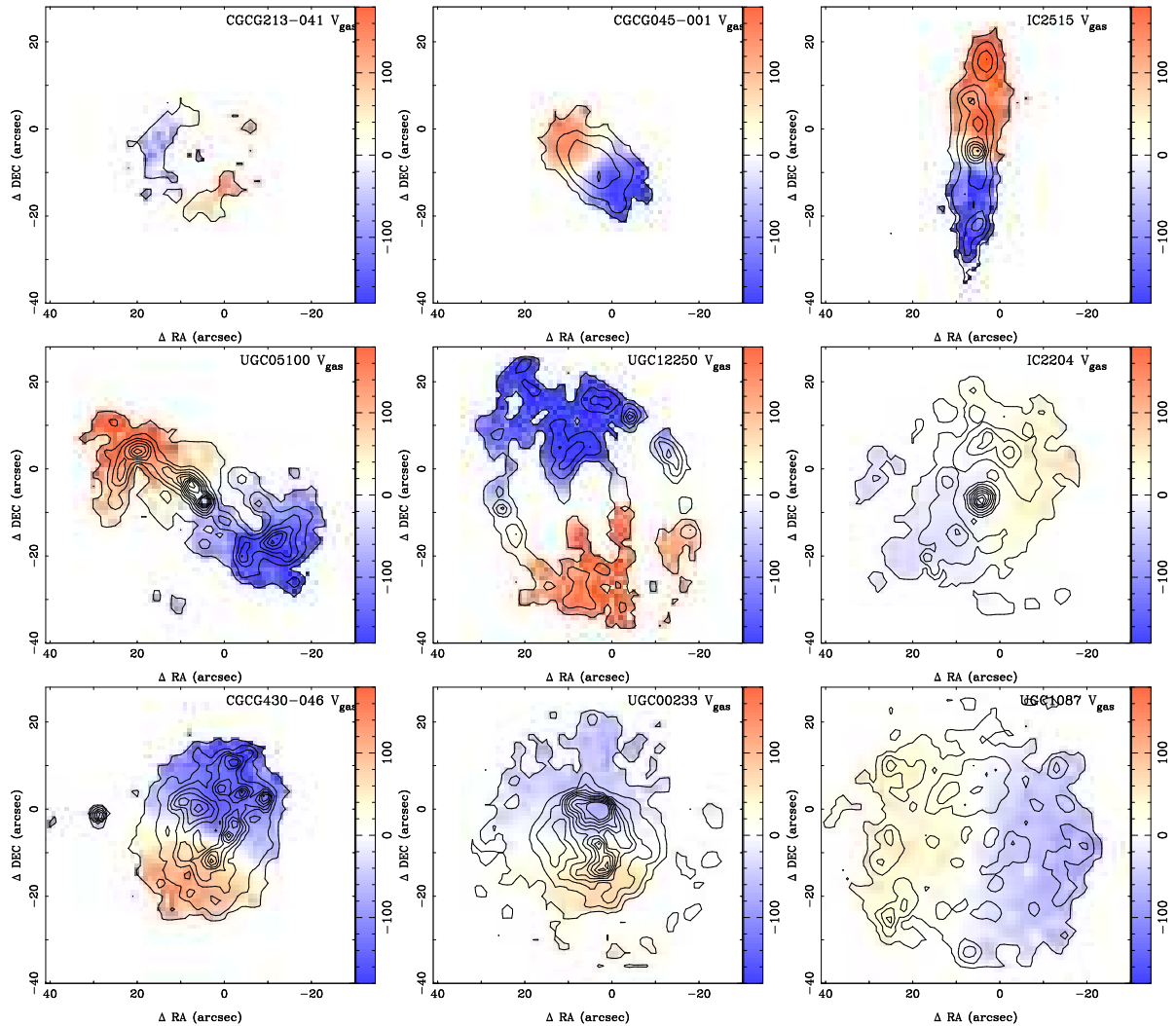


Fig. 19. For the same sub-set of galaxies than in previous figures, colour map of the velocity obtained from the $H\alpha$ emission, once corrected by the corresponding systemic velocity. The black solid contours shows the $H\alpha$ observed intensity, starting at $0.3 \cdot 10^{-16} \text{ erg s}^{-1} \text{ cm}^{-2}$, and with a step of $1 \cdot 10^{-16} \text{ erg s}^{-1} \text{ cm}^{-2}$ for each contour, as in Fig. 18.

Two sample selections have been explored, based on (1) a pure redshift selection and (2) a diameter selected sample, and two different instrumental setups has been adopted, covering in both cases a similar FOV of $\sim 1 \text{ arcmin}^2$ and spectral range ($\sim 3700 - 7050 \text{ \AA}$), but with different spectral resolutions: $R \sim 500$ and $R \sim 900$. We show that it is possible to adopt a fix instrumental setup and observing strategy to observe a large sample of nearby galaxies in a reasonable amount of time (i.e., a couple of hours per target, including overheads), covering most of the optical extension of these galaxies and wide spectroscopic optical range with PPAK.

We present a detailed description of the data reduction, and we demonstrate that the large amount of data produced in this kind of observations can be handled if a dedicated automatic reduction pipeline is implemented. In addition, an automatic analysis procedure is used to handle the large number of spectra in the datacubes derived for each individual galaxy, and to obtain the their physical properties.

We perform a set of simulations to explore the accuracy of the physical properties derived from the data. These simulations indicate that the adopted observational strategy, and in particular, the adopted resolutions and integration times are suitable to study both the integrated and spatially resolved spectroscopic

properties of these galaxies. The simulations show that the spectral range of the data is not wide enough to determine simultaneously the dust attenuation and the stellar populations, and additional information from other spectral bands, as UV and infrared, is needed to break the age-metallicity-dust degeneration. The recovering of the properties of the ionised gas and the kinematics is well performed with the simple grid of templates used here, although the determination of the luminosity-weighted age and, especially, metallicity depends on the grid of templates used, as expected.

From the comparison of the galaxy data of this work with previously published imaging and spectroscopic data from the SDSS survey, we show that it is feasible (1) to obtain spectrophotometric calibrated IFS spectra, and (2) the derived spectroscopic properties are recovered equally well than with single fiber spectra. A showcase analysis of the two dimensional properties for a sub-set of galaxies of this sample indicates that it is feasible to derive the spectroscopic properties for different apertures, and to obtain accurate 2D distributions of these properties within the optical extension of these galaxies.

Finally, we want to highlight that Integral Field Spectroscopy constitutes a powerful approach for the understanding of the global evolution of nearby galaxies from the analysis of their

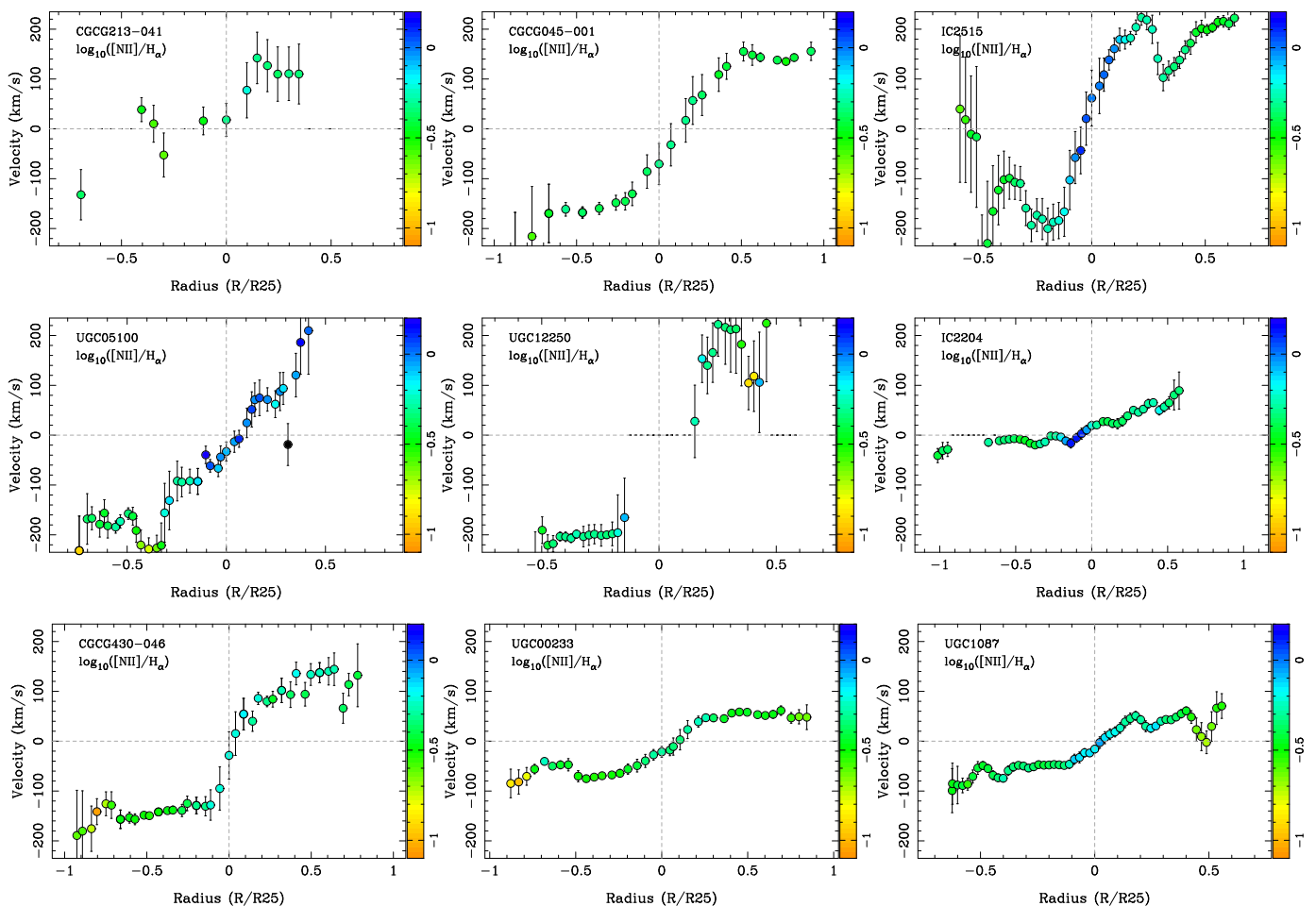


Fig. 20. Rotational curves derived from the maps shown in the previous figure along the axis of maximum rotation. The colour code indicates the $[\text{N II}]\lambda 6583/\text{H}\alpha$ ratio, in logarithmic scale. The distances are normalised by the R_{25} radius.

resolved physical properties. This study was part of the preparatory works for a larger IFS survey, the CALIFA survey¹² (~ 600 galaxies at $0.005 < z < 0.030$), which will be an important resource for detailed studies of galaxies in the Local Universe.

Acknowledgements. We thank the referee, Matt Bershadly, for his useful comments. We acknowledge the *Viabilidad, Diseño, Acceso y Mejora* funding program, ICTS-2009-10, and the *Plan Nacional de Investigación y Desarrollo* funding program AYA2010-22111-C03-03 and AYA-2010-10904-E, of the Spanish Ministerio de Ciencia e Innovación (MICINN), for the support given to this project. EMQ acknowledges financial support from the research projects AYA2007-67752-C03-03 and AYA2010-21322-C03-02. EMQ, RM and AGP thank support from Consolider-GTC and AstroMadrid S2009/ESP-1496 – from the Comunidad de Madrid –. RM and AGP acknowledge financial support from the project AYA2005-09413-C02-02. JVM and JIP are funded by the grants AYA2007-67965-C03-02 – from the Spanish MICINN – and TIC114 – from the Junta de Andalucía –.

We also thank the director of CEFCA, Dr. M. Moles, for his sincere support to this project.

This paper makes use of the Sloan Digital Sky Survey data. Funding for the SDSS and SDSS-II has been provided by the Alfred P. Sloan Foundation, the Participating Institutions, the National Science Foundation, the U.S. Department of Energy, the National Aeronautics and Space Administration, the Japanese Monbukagakusho, the Max Planck Society, and the Higher Education Funding Council for England. The SDSS Web Site is <http://www.sdss.org/>.

The SDSS is managed by the Astrophysical Research Consortium for the Participating Institutions. The Participating Institutions are the American Museum of Natural History, Astrophysical Institute Potsdam, University of Basel, University of Cambridge, Case Western Reserve University, University of Chicago, Drexel University, Fermilab, the Institute for Advanced Study,

the Japan Participation Group, Johns Hopkins University, the Joint Institute for Nuclear Astrophysics, the Kavli Institute for Particle Astrophysics and Cosmology, the Korean Scientist Group, the Chinese Academy of Sciences (LAMOST), Los Alamos National Laboratory, the Max-Planck-Institute for Astronomy (MPIA), the Max-Planck-Institute for Astrophysics (MPA), New Mexico State University, Ohio State University, University of Pittsburgh, University of Portsmouth, Princeton University, the United States Naval Observatory, and the University of Washington.

References

- Bacon, R., Copin, Y., Monnet, G., et al. 2001, *MNRAS*, 326, 23
 Bell, E. F., McIntosh, D. H., Barden, M., et al. 2004, *ApJ*, 600, L11
 Bell, E. F., Naab, T., McIntosh, D. H., et al. 2006, *ApJ*, 640, 241
 Bershadly, M. A., Andersen, D. R., Harker, J., Ramsey, L. W., & Verheijen, M. A. W. 2004, *PASP*, 116, 565
 Bershadly, M. A., Andersen, D. R., Verheijen, M. A. W., et al. 2005, *ApJS*, 156, 311
 Bershadly, M. A., Verheijen, M. A. W., Swaters, R. A., et al. 2010a, *ApJ*, 716, 198
 Bershadly, M. A., Verheijen, M. A. W., Westfall, K. B., et al. 2010b, *ApJ*, 716, 234
 Blanc, G. A., Gebhardt, K., Heiderman, A., et al. 2010, *ArXiv e-prints*
 Calzetti, D. 2001, *PASP*, 113, 1449
 Cappellari, M., Emsellem, E., Krajnović, D., et al. 2011, *MNRAS*, 269
 Cardelli, J. A., Clayton, G. C., & Mathis, J. S. 1989, *ApJ*, 345, 245
 Castillo-Morales, A., Gallego, J., Pérez-Gallego, J., et al. 2010, in *Highlights of Spanish Astrophysics V*, ed. J. M. Diego, L. J. Goicoechea, J. I. González-Serrano, & J. Gorgas, 267
 Charlot, S. & Fall, S. M. 2000, *ApJ*, 539, 718
 Chen, Y., Lowenthal, J. D., & Yun, M. S. 2010, *ApJ*, 712, 1385

¹² <http://www.caha.es/CALIFA/>

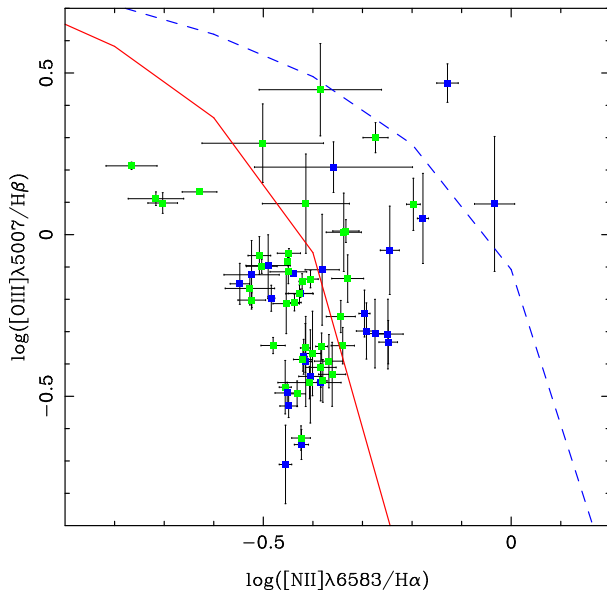


Fig. 17. The BPT diagnostic diagram for the central (blue filled squares) and integrated (green filled circles) spectra for the galaxies in the sample. The blue dashed and red solid lines separate the zones of HII-like galaxies (below the lines) and AGNs (above the lines) as defined by Kauffmann et al. (2003) and Kewley et al. (2001), respectively.

- Sánchez, S. F., Aceituno, J., Thiele, U., Pérez-Ramírez, D., & Alves, J. 2007a, *PASP*, 119, 1186
- Sánchez, S. F., Cardiel, N., Verheijen, M. A. W., Pedraz, S., & Covone, G. 2007b, *MNRAS*, 376, 125
- Sánchez, S. F., Kennicutt, R. C., Gil de Paz, A., et al. 2011a, *A&A*, submitted
- Sánchez, S. F., Kennicutt, R. C., Gil de Paz, A., et al. 2010, *ArXiv e-prints*
- Sánchez, S. F., Rosales-Ortega, F. F., Kennicutt, R. C., et al. 2011b, *MNRAS*, 410, 313
- Sandage, A. 1986, *A&A*, 161, 89
- Sarzi, M., Falcón-Barroso, J., Davies, R. L., et al. 2006, *MNRAS*, 366, 1151
- Skrutskie, M. F., Cutri, R. M., Stiening, R., et al. 2006, *AJ*, 131, 1163
- Strateva, I., Ivezić, Ž., Knapp, G. R., et al. 2001, *AJ*, 122, 1861
- Vazdekis, A., Sánchez-Blázquez, P., Falcón-Barroso, J., et al. 2010, *MNRAS*, 404, 1639
- Veilleux, S. & Osterbrock, D. E. 1987, *ApJS*, 63, 295
- Verheijen, M. A. W., Bershady, M. A., Andersen, D. R., et al. 2004, *Astronomische Nachrichten*, 325, 151
- Viironen, K., Sánchez, S. F., Mármol-Queralto, E., et al. 2011, *A&A*, submitted

- Cid Fernandes, R., Mateus, A., Sodré, L., Stasińska, G., & Gomes, J. M. 2005, *MNRAS*, 358, 363
- Cusumano, G., La Parola, V., Segreto, A., et al. 2010, *A&A*, 510, A48+
- de Zeeuw, P. T., Bureau, M., Emsellem, E., et al. 2002, *MNRAS*, 329, 513
- Faber, S. M., Willmer, C. N. A., Wolf, C., et al. 2007, *ApJ*, 665, 265
- Gavazzi, G., Bonfanti, C., Sanvito, G., Boselli, A., & Scodreggio, M. 2002, *ApJ*, 576, 135
- Gil de Paz, A., Boissier, S., Madore, B. F., et al. 2007, *ApJS*, 173, 185
- Hardcastle, M. J., Kraft, R. P., Worrall, D. M., et al. 2007, *ApJ*, 662, 166
- Helmboldt, J. F., Walterbos, R. A. M., Bothun, G. D., O’Neil, K., & de Blok, W. J. G. 2004, *ApJ*, 613, 914
- Hill, G. J., MacQueen, P. J., Smith, M. P., et al. 2008, in *Society of Photo-Optical Instrumentation Engineers (SPIE) Conference Series*, Vol. 7014, Society of Photo-Optical Instrumentation Engineers (SPIE) Conference Series
- Hinshaw, G., Weiland, J. L., Hill, R. S., et al. 2009, *ApJS*, 180, 225
- Jenkins, E. B. 1987, in *Astrophysics and Space Science Library*, Vol. 134, *Interstellar Processes*, ed. D. J. Hollenbach & H. A. Thronson Jr., 533–559
- Jester, S., Schneider, D. P., Richards, G. T., et al. 2005, *AJ*, 130, 873
- Karachentsev, I. D. & Kaisin, S. S. 2010, *AJ*, 140, 1241
- Kauffmann, G., Heckman, T. M., Tremonti, C., et al. 2003, *MNRAS*, 346, 1055
- Kelz, A., Verheijen, M. A. W., Roth, M. M., et al. 2006, *PASP*, 118, 129
- Kennicutt, Jr., R. C., Lee, J. C., Funes, José G., S. J., Sakai, S., & Akiyama, S. 2008, *ApJS*, 178, 247
- Kewley, L. J., Dopita, M. A., Sutherland, R. S., Heisler, C. A., & Trevena, J. 2001, *ApJ*, 556, 121
- Koleva, M., Prugniel, P., Bouchard, A., & Wu, Y. 2009, *A&A*, 501, 1269
- Lasker, B. M., Lattanzi, M. G., McLean, B. J., et al. 2008, *AJ*, 136, 735
- MacArthur, L. A., González, J. J., & Courteau, S. 2009, *MNRAS*, 395, 28
- Meurer, G. R., Hanish, D. J., Ferguson, H. C., et al. 2006, *ApJS*, 165, 307
- Monet, D. G., Levine, S. E., Canzian, B., et al. 2003, *AJ*, 125, 984
- Muñoz-Mateos, J. C., Gil de Paz, A., Boissier, S., et al. 2009, *ApJ*, 701, 1965
- Muñoz-Mateos, J. C., Gil de Paz, A., Boissier, S., et al. 2007, *ApJ*, 658, 1006
- Ocvirk, P., Pichon, C., Lançon, A., & Thiébaud, E. 2006, *MNRAS*, 365, 46
- Oke, J. B. 1990, *AJ*, 99, 1621
- Pérez-Gallego, J., Guzmán, R., Castillo-Morales, A., et al. 2010, *MNRAS*, 402, 1397
- Pérez-González, P. G., Zamorano, J., Gallego, J., Aragón-Salamanca, A., & Gil de Paz, A. 2003, *ApJ*, 591, 827
- Rosales-Ortega, F. F., Kennicutt, R. C., Sánchez, S. F., et al. 2010, *MNRAS*, 405, 735
- Roth, M. M., Kelz, A., Fechner, T., et al. 2005, *PASP*, 117, 620
- Sánchez, S. F. 2004, *Astronomische Nachrichten*, 325, 167
- Sánchez, S. F. 2006, *Astronomische Nachrichten*, 327, 850